Draft version February 1, 2022
Preprint typeset using LaTeX style emulateapj v. 12/16/11

GRB 170817A ASSOCIATED WITH GW170817: MULTI-FREQUENCY OBSERVATIONS AND MODELING OF PROMPT GAMMA-RAY EMISSION

A. S. Pozanenko[1,2,3], M. V. Barkov[4,5], P. Yu. Minaev[1], A. A. Volnova[1], E. D. Mazaeva[1], A. S. Moskvitin[6], M. A. Krugov[7], V. A. Samodurov[2,8], V. M. Loznikov[1], and M. Lyutikov[4]

[1]Space Research Institute, 84/32 Profsoyuznaya Street, Moscow 117997, Russia
[2]National Research University Higher School of Economics, Myasnitskaya 20, 101000, Moscow, Russia
[3]National Research Nuclear University MEPhI (Moscow Engineering Physics Institute), Kashirskoe shosse, 31, 115409 Moscow, Russia
[4]Department of Physics and Astronomy, Purdue University, 525 Northwestern Avenue, West Lafayette, IN 47907-2036, USA
[5]Astrophysical Big Bang Laboratory, RIKEN, 2-1 Hirosawa, Wako, Saitama 351-0198, Japan
[6]Special Astrophysical Observatory of Russian Academy of Sciences, Nizhniy Arkhyz, 369167, Russia
[7]Fesenkov Astrophysical Institute, Almaty, 050020, Kazakhstan
[8]Pushchino Radio Astronomy Observatory ASC LPI, Pushchino, Russia

Draft version February 1, 2022

Abstract

We present our observations of electromagnetic transients associated with GW170817/GRB 170817A using optical telescopes of Chilescope observatory and Big Scanning Antenna (BSA) of Pushchino Radio Astronomy Observatory at 110 MHz. The Chilescope observatory detected an optical transient of $\sim 19^m$ on the third day in the outskirts of the galaxy NGC 4993; we continued observations following its rapid decrease. We put an upper limit of 1.5×10^4 Jy on any radio source with a duration of 10–60 s which may be associated with GW170817/GRB 170817A. The prompt gamma-ray emission consists of two distinctive components - a hard short pulse delayed by ~ 2 seconds with respect to the LIGO signal and softer thermal pulse with $T \sim 10$ keV lasting for another ~ 2 seconds. The appearance of a thermal component at the end of the burst is unusual for short GRBs. Both the hard and the soft components do not satisfy the Amati relation, making GRB 170817A distinctively different from other short GRBs. Based on gamma-ray and optical observations, we develop a model for the prompt high-energy emission associated with GRB 170817A. The merger of two neutron stars creates an accretion torus of $\sim 10^{-2} M_\odot$, which supplies the black hole with magnetic flux and confines the BlandfordZnajek-powered jet. We associate the hard prompt spike with the quasispherical breakout of the jet from the disk wind. As the jet plows through the wind with subrelativistic velocity, it creates a radiation-dominated shock that heats the wind material to tens of kiloelectron volts, producing the soft thermal component.

Subject headings: gravitational waves, gamma-ray burst: individual (GRB 170817A), accretion, accretion disks, techniques: photometric, radio continuum: general

1. INTRODUCTION

On 2017 August 17 at 12:41:04 UTC, the LIGO-Hanford detector triggered the gravitational-wave (GW) transient GW170817 (LIGO Scientific Collaboration & Virgo Collaboration 2017). The GW signal was also found in the data of other LIGO and Virgo detectors and was consistent with the coalescence of a binary neutron star system. Two seconds later (UTC 2017 August 17 12:41:06) GRB 170817A was registered by GBM/*Fermi* (Goldstein et al. 2017a,b; Connaughton et al. 2017) and SPI-ACS/INTEGRAL (Savchenko et al. 2017a,b) experiments. The GBM/*Fermi* localization area of GRB 170817A includes the much smaller localization region of GW170817. A search for the optical counterpart started immediately and was carried out by a large number of ground-based facilities (LIGO Scientific Collaboration et al. 2017).

2. OPTICAL OBSERVATIONS

The optical transient corresponding to the GW170817 and GRB 170817A was discovered independently by several observatories. The first team to discover and report the detection of the optical counterpart was The One-Meter, Two-Hemisphere (1M2H) group. They detected a bright uncatalogued source within the halo of the galaxy NGC4993 in their *i*-band image obtained on 2017 August 17 23:33 UTC with the 1m Swope telescope at Las Campanas Observatory in Chile. This source was labeled as Swope Supernova Survey 2017a (SSS17a; Coulter et al. 2017, notice time 2017 August 17 01:05 UTC). SSS17a (now with the IAU designation AT2017gfo) had coordinates RA(J2000.0) = $13^h09^m48\overset{s}{.}085 \pm 0\overset{s}{.}018$, Dec(J2000.0) = $-23°22'53\overset{''}{.}343 \pm 0\overset{''}{.}218$ and was located at a projected distance of $10\overset{''}{.}6$ from the center of NGC 4993, an early-type galaxy at a distance of $\simeq 40$ Mpc. Hereafter, we refer to the optical counterpart as OT.

The Distance Less Than 40 Mpc survey (DLT40; Tartaglia et al. 2017, in preparation) obtained their first image of NGC 4993 region on 2017 August 17 23:50 UTC and independently detected the transient, automatically labeled DLT17ck (Yang et al. 2017, notice time August 18, 01:41 UTC).

MASTER-OAFA robotic telescope (Lipunov et al. 2010) observed the region including NGC 4993 on August 17 23:59 UTC, and the automated software independently detected the transient labeled MASTER OT J130948.10-232253.3 (Lipunov et al. 2017, notice time August 18, 05:38 UTC).

Visible and Infrared Survey Telescope for Astronomy (VISTA) also observed the transient SSS17a/DLT17ck/MASTER OT J130948.10-232253.3 in the infrared band on August 18, 00:10 UT (Tanvir & Levan 2017, notice time August 18, 05:04 UTC).

Las Cumbres Observatory (LCO; Brown et al. 2013) surveys started observations of the *Fermi* localization region immediately after the corresponding GCN circular distribution. Approximately 5 hr later, when the LIGO-Virgo localization map was issued, the observations were switched to the priority list of galaxies (Dalya et al. 2016). On August 18 00:15 UTC, a new transient near NGC 4993 was detected at the position corresponding to the OT (Arcavi et al. 2017, notice time August 18, 04:07 UTC).

The team of DECam on the 4 m telescope of Cerro Tololo Inter-American Observatory independently detected in optics the new source north and east of NGC 4993 in the frame taken on August 18, 00:42 UTC (Allam et al. 2017, notice time August 18, 01:15 UTC).

We started observations of the error box of GW170817 (LIGO/Virgo trigger G298048) on August 17 23:17:16 UTC (Pozanenko et al. 2017a, notice time August 18, 14:24 UTC) with the facilities of the Chilescope observatory (see Appendices A.1 and A.2). Simultaneously, we started mosaic observations of GBM/*Fermi* localization area of GRB 170817A (von Kienlin et al. 2017) taking a series of spatially tiled images with another instrument of the same observatory (see Appendix A.3). The observations ended ~ 5 minutes before the GCN circular about the discovery of the transient was distributed by Swope (Coulter et al. 2017). The location of the NGC 4993 was out of the covered fields of our first observational set.

We started to observe the optical counterpart of the GW170817 (LIGO Scientific Collaboration & Virgo Collaboration 2017) labeled SSS17a (Coulter et al. 2017) on 2017 August 19 at 23:30:33 with RC-1000 telescope of Chilescope observatory (Pozanenko et al. 2017b) and continued observations on 2017 August 20, 21, and 24. Details of our optical observations and data reduction are presented in Appendices A.4 and A.5. The final light curve in the R-filter incorporating our photometry result are presented in the Appendix A.6. We also compared the light curves of the afterglow of GRB 130603B with the light curve of the optical counterpart of GRB 170817A and found that afterglow luminosity of GRB 170817A is more than 130 times fainter than that of GRB 130603B in *J*-filter (see A.6). We used data of the Big Scanning Antenna (BSA) radio telescope survey at 110 MHz to estimate the possible radio prompt emission. Details of our radio observations are presented in Appendix B.

3. GRB 170817A PROMPT GAMMA-RAY DATA ANALYSIS

3.1. *SPI-ACS/INTEGRAL*

The description of GRB 170817A INTEGRAL observations and detailed analysis of the burst based on INTEGRAL data are presented in Savchenko et al. (2017a). We performed a basic analysis of the SPI AntiCoincidence Shield (SPI-ACS) data with a slightly different method to classify the burst and to estimate its energetics, and then compare our results with those of GBM/*Fermi* in order to calibrate SPI-ACS consequently. We found the burst to be from a short (or Type I) population with no precursor and extended emission components. Derived values of fluxes in energetic units are consistent with both our GBM/*Fermi*, and Savchenko et al. (2017a) results. The time delay between the burst onset and GW trigger was found to be $\simeq 2$ s. The background-subtracted light curve of the burst in SPI-ACS data with a time resolution of 0.2 s is shown in Figure 1 (panel e). The details of the analysis are presented in Appendix C.

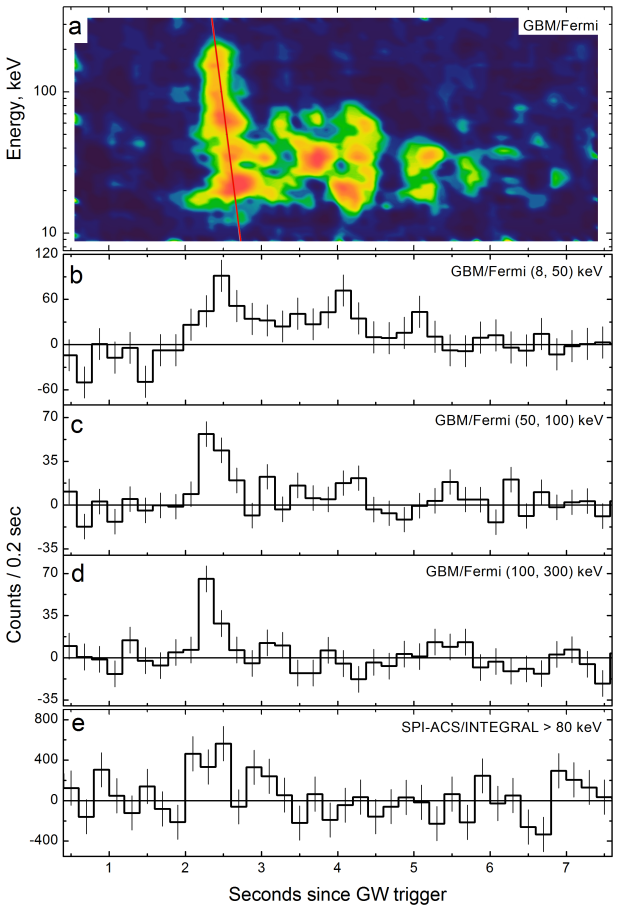

FIG. 1.— Background-subtracted dynamic count spectrum (a) and light curves of GRB 170817A in data of GBM/*Fermi* (NaI: 1, 2, 5) in (8, 50) keV (b), (50, 100) keV (c), (100, 300) keV (d), and in data of SPI-ACS/INTEGRAL (e). Time in seconds since GW trigger (UTC 2017 August 17 12:41:04) is on the X-axis, counts over 0.2 s time bins are on the Y-axis for light curves. Flux uncertainties are presented at the 1σ significance level. A warmer color on the dynamic count spectrum (a) corresponds to a higher flux. The two-component (pulse) structure of GRB 170817A is seen. For the first pulse, red line represents logarithmic spectral lag behavior on energy, $lag \sim 0.24 \times log(E)$. The logarithmic approximation is typical for single pulses of GRBs (Minaev et al. 2014).

3.2. *GBM/Fermi*

We used the publicly accessible FTP archive [1] as the source of the GBM/*Fermi* data.

GRB 170817A was detected in GBM/*Fermi* (NaI: 1, 2, 5) at the 8.7σ significance level in the (8, 300) keV energy range. The background-subtracted dynamic count spectrum in the (8, 400) keV range and light curves of the

[1] `ftp://legacy.gsfc.nasa.gov/fermi/data/`

burst with time resolution of 0.2 s are presented in three energy channels in panels (a)–(d) in Figure 1. The burst onset in GBM/*Fermi* data is delayed by $\simeq 2$ s compared to the GW trigger. The third-order polynomial model was used to fit background in time intervals (-40, -5) and (20, 70) s for all presented GBM/*Fermi* light curves.

As seen in Figure 1, light curve of the burst consists of two different components (pulses): the first one is short hard and the second one is visible only in soft energy range the (8, 50) keV. The two-component structure of the burst is also confirmed by T_{90} duration parameter values: in the (8, 70) keV energy range $T_{90}^{8-70\ keV} = 2.9 \pm 0.3$ s, which is six times longer than the duration in the (70, 300) keV energy range, $T_{90}^{70-300\ keV} = 0.5 \pm 0.1$ s. (That behavior cannot be explained by the well-known dependence of GRB duration on energy range, $T_{90} \propto E^{-0.4}$; see, e.g., Fenimore et al. 1995; Minaev et al. 2010b).

To construct and fit the energy spectra, we used the RMfit v4.3.2 software package[2] developed to analyze the GBM data of the *Fermi* observatory. The method of spectral analysis is similar to that proposed by Gruber et al. (2014), who also used the RMfit software package. To fit the energy spectra and to choose an optimal spectral model, we used modified Cash statistics (C-Stat; see Cash 1979).

Results of spectral analysis performed for GRB 170817A using data of GBM/*Fermi* (NaI: 1, 2, 5, BGO: 0) are summarized in Table 1. We analyzed three time intervals covering the whole burst — (-0.3, 2.0) s since GBM trigger, the first hard pulse (-0.3, 0.3) s, and the second soft pulse (0.8, 2.0) s — with three spectral models — power law (PL), power law with exponential cutoff (CPL), and thermal model (BB). To choose the optimal spectral model, we used the ΔC-Stat $> \Delta$C-Stat$_{\rm crit}$ criterion, where ΔC-Stat is the difference between C-Stat values obtained for various models (the last column in Table 1) and ΔC-Stat$_{\rm crit} \simeq 8.5$ was obtained via simulations in Gruber et al. (2014) for PL versus CPL model comparison.

The energetic spectrum of the whole burst (time interval (-0.3, 2.0) s) is best fitted by the CPL model with $\alpha = -0.5^{+0.9}_{-0.7}$ and $E_{\rm peak} = 65^{+35}_{-14}$ keV (the improvement over PL model is ΔC-Stat = 10). The fluence in the (10, 1000) keV range is $F = (2.1 \pm 0.3) \times 10^{-7}$ erg cm^{-2}. Using the CPL spectral model, we calculated the hardness ratio of photon fluxes between (50, 300) keV and (15, 50) keV energy bands, HR $= 0.46 \pm 0.09$, which, along with duration $T_{90}^{70-300\ keV} = 0.5 \pm 0.1$ s, characterizes the burst to be a typical short but soft one (e.g., see Fig. 6 in von Kienlin et al. 2014). The probability that GRB 170817A is from the short population was estimated using duration and hardness values in Goldstein et al. (2017a) and found to be $P \simeq 73\%$.

The optimal spectral model for the first pulse (time interval (-0.3, 0.3) s) of the GRB 170817A is the CPL model (Table 1) with $\alpha = -0.9 \pm 0.4$ and $E_{\rm peak} = 230^{+310}_{-80}$ keV (the improvement over the PL model is ΔC-Stat = 9). Using the CPL spectral model, we calculated a hardness ratio between (50, 300) keV and (15, 50) keV energy bands, HR $= 1.0 \pm 0.2$, which describes the first pulse as a hard one (see Fig. 6 in von Kienlin et al. 2014).

[2] http://fermi.gsfc.nasa.gov/ssc/data/analysis/rmfit/

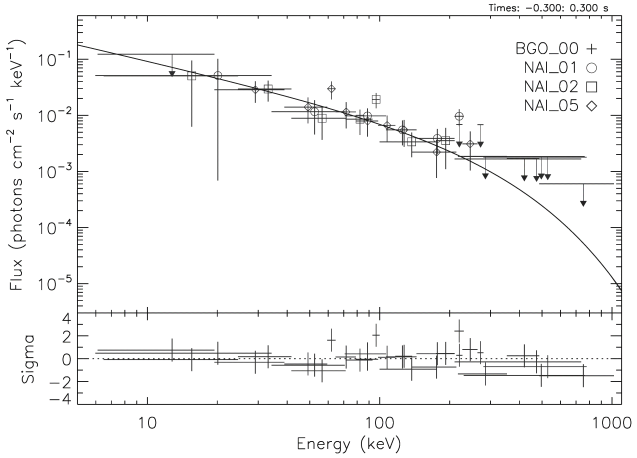

FIG. 2.— Photon spectrum (upper panel) and residuals (lower panel) of the CPL spectrum model for the first pulse.

The optimal spectral model for the second pulse (time interval (0.8, 3.0) s) of the GRB 170817A is a thermal model with $kT = 11.2 \pm 1.5$ keV and the fluence is in the (10, 1000) keV energy range of $F = (6.8 \pm 1.1) \times 10^{-8}$ erg cm^{-2} (Table 1). The CPL model gives the same goodness of fit, but with a positive value of $\alpha = 2.3^{+4.5}_{-1.9}$, bringing this model maximally close to Wien's law $N_E \sim E^2 exp(-E/kT)$ — the spectral shape that the radiation originating in an optically thick hot medium whose opacity is dominated by Compton scattering off electrons acquires (Kompaneets 1957), which also confirms the thermal nature of the second pulse. The $E_{\rm peak}$ parameter was found to be $E_{\rm peak} = 43^{+9}_{-7}$ keV within the CPL model. The improvement of C-Stat for CPL and BB models comparing to the PL one is ΔC-Stat = 17, which is two times larger than ΔC-Stat$_{\rm crit} \simeq 8.5$ found in Gruber et al. (2014) and used as model selection criterion. Within the CPL model, the hardness ratio between (50, 300) keV and (15, 50) keV energy bands, HR $= 0.23 \pm 0.10$, which describes the second pulse to be a very soft one (see Fig. 6 in von Kienlin et al. (2014)).

Optimal spectral models are presented in Figures 2 and 3, while confidence regions of the parameters of CPL models for both pulses are presented in Figure 4. As can be seen from Figure 4, the spectrum describing these two pulses is not evolving, but rather is a manifestation of the different nature of the emission. The results of our spectral analysis are comparable with ones presented in Goldstein et al. (2017a).

We did not find any precursor or extended emission components in GBM/*Fermi* data at time scales from 0.1 up to 20 s in the time interval (-10, 30) s since GBM triggers in the energy range of (8, 300) keV. To estimate upper limits on their intensity in energetic units, we derived a conversion factor in the (8, 300) keV range using count fluence of the burst and energetic fluence within the CPL spectral model (Table 1). We found that 1 count in GBM/*Fermi* corresponds to $\sim 3.2 \times 10^{-10}$ erg cm^{-2} in an energy range of (8, 300) keV. At a time scale of 0.1 s, the upper limit on precursor activity is

TABLE 1
Results of Spectral Analysis of GRB 170817A Based on GBM/*Fermi* Data

Time Interval [a] (s)	Model [b]	α	$E_{\rm peak}$ [c] (keV)	Fluence [d] (10^{-7} erg cm^{-2})	Hardness Ratio [e]	C-Stat/dof
(-0.3, 0.3)	PL	-1.50 ± 0.08	-	2.8 ± 0.4	0.72 ± 0.13	425/367
first	BB	-	31.6 ± 3.2	1.4 ± 0.2	2.8 ± 0.6	437/367
pulse	CPL ⋆	-0.9 ± 0.4	230^{+310}_{-80}	2.2 ± 0.5	1.0 ± 0.2	416/366
(0.8, 2.0)	PL	-2.0 ± 0.3	-	1.0 ± 0.4	0.37 ± 0.15	439/367
second	BB ⋆	-	11.2 ± 1.5	0.68 ± 0.11	0.24 ± 0.09	422/367
pulse	CPL	$2.3^{+4.5}_{-1.9}$	43^{+9}_{-7}	0.67 ± 0.12	0.23 ± 0.10	422/366
(-0.3, 2.0)	PL	-1.8 ± 0.1	-	3.7 ± 0.7	0.49 ± 0.09	450/367
whole	BB	-	13.3 ± 1.3	1.7 ± 0.2	0.39 ± 0.08	447/367
burst	CPL ⋆	$-0.5^{+0.9}_{-0.7}$	65^{+35}_{-14}	2.1 ± 0.3	0.46 ± 0.09	440/366

[a] Time interval relative to GBM trigger (UTC 2017 August 17 12:41:06.475).
[b] PL is for power law, CPL is for power law with an exponential cutoff, and BB is for a thermal model.
[c] For the BB spectral model, the $E_{\rm peak}$ column gives the parameter kT.
[d] Fluence in the (10, 1000) keV energy range.
[e] Hardness ratio calculated as a ratio of photon fluxes in the (50, 300) keV and the (15, 50) keV energy bands.
⋆ Optimal spectral model.

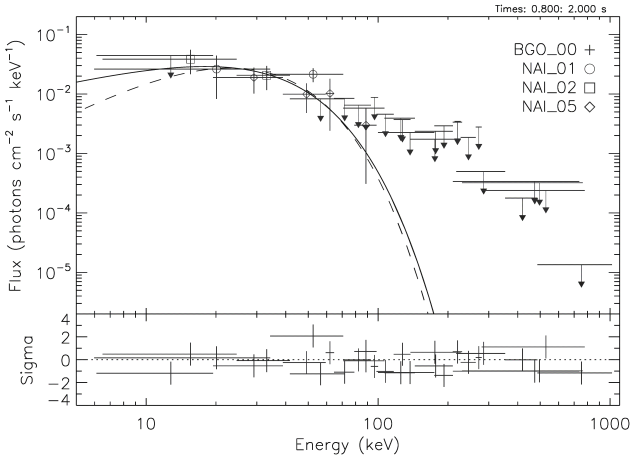

Fig. 3.— Photon spectrum (upper panel) and residuals (lower panel) of the black body spectrum model for the second pulse. The dashed line represents the CPL fit of the photon spectrum.

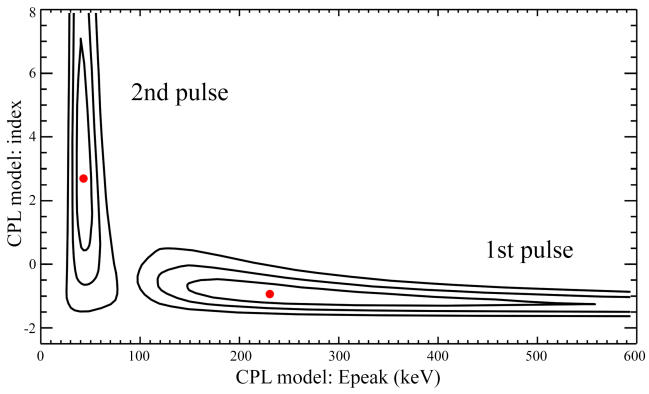

Fig. 4.— Confidence regions at the 1, 2, 3σ levels of the CPL spectrum parameters (power-law index, α and $E_{\rm peak}$) for the first and second pulses.

$S_{\rm prec} \simeq 1.6 \times 10^{-8}$ erg cm^{-2} at the 3σ significance level. At a time scale of 20 s, upper limit on extended emission activity is $S_{\rm EE} \simeq 2.3 \times 10^{-7}$ erg cm^{-2} at a the 3σ significance level. The upper limits are two times deeper than ones obtained with SPI-ACS (see Appendix C).

A spectral lag analysis based on the CCF method (see, e.g., Minaev et al. 2014) was performed for GRB 170817A using the light curves detected by GBM/*Fermi* (NaI: 1, 2, 5) in the energy bands (8, 50) keV, (50, 100) keV, and (100, 300) keV with a time resolution of 0.04 s. The spectral lag between (8, 50) keV and (50, 100) keV bands is negligible, lag $= 0.01 \pm 0.08$ s, but between (8, 50) keV and (100, 300) keV lag is significant, lag $= 0.27 \pm 0.05$ s. It might represent the hard-to-soft spectral evolution of the first pulse (see Figure 1, upper panel).

3.3. *Amati Relation*

One of the interesting phenomenological relations for GRBs is the Amati diagram, i.e., the dependence of the equivalent isotropic energy $E_{\rm iso}$ emitted in gamma-rays between (1, 10,000) keV on parameter $E_{\rm peak}(1+z)$ in the source frame (Amati 2010), which can also be used for the classification of GRBs (see, e.g., Qin & Chen 2013).

Using the experimental data given in Svinkin et al. (2016); Qin & Chen (2013); Minaev & Pozanenko (2017) we constructed the Amati diagram for 20 short bursts and fitted the relation with a power-law-like logarithmic model: $\log\left(\frac{E_{\rm peak}(1+z)}{1\ {\rm keV}}\right) = (0.50 \pm 0.04) \log\left(\frac{E_{\rm iso}}{1{\rm erg}}\right) + (-22.4 \pm 1.8)$. Details on the investigation of the Amati relation for short GRBs can be found elsewhere (P. Minaev 2018, in preparation).

Using optimal spectral models derived in the previous subsection for GRB 170817A (Table 1) and assuming a redshift of z = 0.00968 and a luminosity distance of $D_L =$ 42.0 Mpc for the source (Jones et al. 2009), we estimated $E_{\rm iso}$ and $L_{\rm iso}$ parameters in the (1, 10,000) keV range (Table 2). All burst components (first, second pulses, and the whole burst) lie far above the 2σ correlation region (Figure 5).

If we assume that the burst GRB 170817A should obey the Amati relation, we can draw a trajectory of the burst parameters as $E_p \sim E_{\rm iso}^{1/3}$ if it is a cone relativistic jet emission, and $E_p \sim E_{\rm iso}^{1/4}$ if it is a spherical relativistic emission (see, e.g., Eichler & Levinson 2004; Levinson & Eichler 2005). One can see that neither of the trajectories cross the Amati relation at a reasonable $E_{\rm iso}$, especially for the first pulse. This strongly supports an alternative explanation for the nature of the first pulse as well as the

TABLE 2
GRB 170817A ENERGETICS

Time Interval [a] (s)	Spectral model [b]	Flux [c] 10^{-7} erg/(cm^2 s)	Fluence [d] 10^{-7} erg cm^{-2}	$E_{\rm iso}$ 10^{46} erg	$L_{\rm iso}$ 10^{46} erg s^{-1}
(-0.3, 0.3)	CPL	3.8 ± 0.9	2.3 ± 0.9	4.9 ± 1.2	8.1 ± 1.9
(0.8, 2.0)	BB	0.59 ± 0.10	0.71 ± 0.12	1.5 ± 0.3	1.3 ± 0.2
(0.8, 2.0)	CPL	0.56 ± 0.10	0.67 ± 0.13	1.4 ± 0.3	1.2 ± 0.2
(-0.3, 2.0)	CPL	0.96 ± 0.14	2.2 ± 0.32	4.7 ± 0.7	2.1 ± 0.3

[a] Relative to the GBM trigger (UTC 2017 August 17 12:41:06.475).
[b] CPL is for power law with an exponential cutoff, BB for a thermal model.
[c] Energy flux in the (1, 10,000) keV energy range.
[d] Energy fluence in the (1, 10,000) keV energy range.

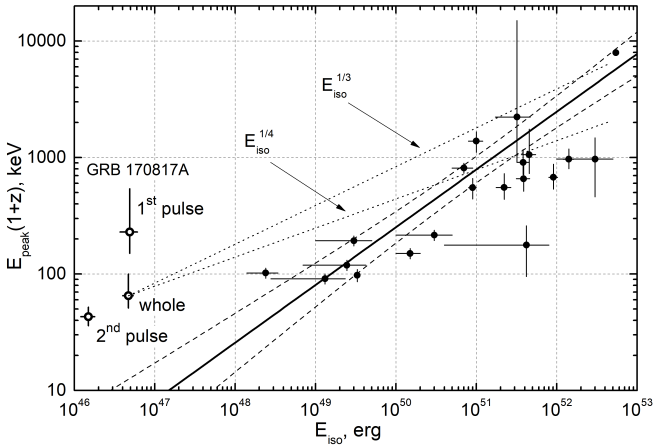

FIG. 5.— Amati diagram; the dependence of the equivalent isotropic energy $E_{\rm iso}$ emitted in the (1, 10000) keV range on $E_{\rm peak}(1+z)$ in the source frame (Amati 2010), for short bursts. A power-law fit (thick solid line) with dashed lines bounding the 2σ region are shown. Dotted lines starting from the point for the whole GRB 170817A indicate the dependence $E_{\rm peak}(1+z) \sim E_{\rm iso}^{1/3}$ and $E_{\rm peak}(1+z) \sim E_{\rm iso}^{1/4}$. Uncertainties for $E_{\rm iso}$ and $E_{\rm peak}(1+z)$ are presented at the 1σ significance level.

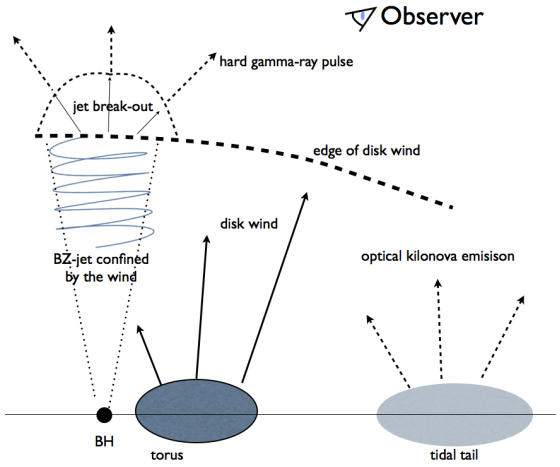

FIG. 6.— Sketch of our scenario. After merging of NSs, a BH is formed, which is surrounded by a compact accretion disk with **intense** wind. After sufficient magnetic flux is accumulated on the BH an electromagnetic jet is launched, confined initially by the disk wind. After propagating with mildly relativistic velocities, the jet breaks out from the wind zone in a semi-isotropic fashion, reaching highly relativistic Lorentz factors. This is the prompt GRB.

whole burst in comparison with the usual short GRBs presented in the Amati relation (Figure 5).

4. THE SCENARIO

The key points of the model are illustrated in Figures 6-7.

The detection of the EM signal contemporaneous with gravitational waves is consistent with the binary NS scenario for short GRBs (Blinnikov et al. 1984; Paczynski 1986a; Eichler et al. 1989a). Qualitatively, the evolution of merging neutron stars follows a well-defined path (*e.g.* Radice et al. 2016; Ruiz et al. 2016; Baiotti & Rezzolla 2017, and many others), though many details, like the effects of different equations of states, various mass ratios, initial spins, and magnetic field evolution, remain to be settled. An active stage of a merger lasts $\sim 10-100$ milliseconds after which the neutron stars collapse into BH. [3] The BH is fairly fast rotating with the Kerr parameter $a \sim 0.7$ (Radice et al. 2016; Ruiz et al. 2016). The mass of the resulting BH is somewhat smaller than the sum of masses due to emission of neutrinos, gravi-

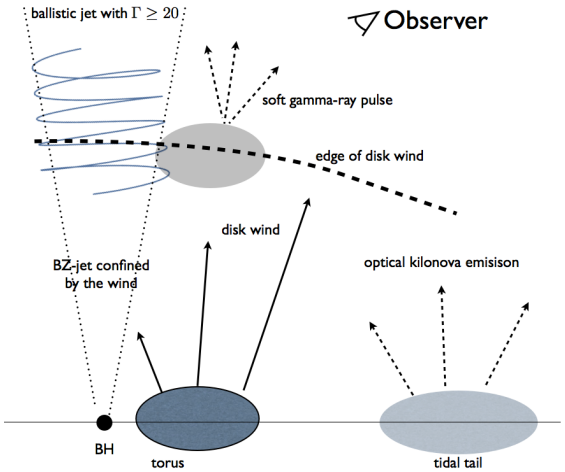

FIG. 7.— Post-breakout structure of the flow. The wind from the disk keeps collimating the jet for a few seconds. The jet propagates ballistically with Lorentz factors ≥ 20 and is unobservable due to deboosting. The shocked wind material produces thermal extended gamma-ray component with $T \sim 10$ keV.

[3] We disfavor alternative scenarios, like the formation of a supermassive fast rotating neutron star with a strong magnetic field (Bisnovatyi-Kogan 1970; LeBlanc & Wilson 1970; Usov 1992; Moiseenko et al. 2006; Metzger et al. 2008b), so we assume the collapse of the very massive neutron star to a BH.

tational waves, ejection of the tidal disruption tail, and wind from the accretion disk, so we can estimate it as $M_{\rm BH} \approx 2.5 M_\odot$. The amount of the ejected material is especially uncertain, but is of utmost importance for the production of the EM signal. It is expected that, first, tidal tails eject $0.01 - 0.03 M_\odot$ with outflow speed $v_{\rm ex} \approx 0.1 - 0.3c$. This material is likely a site of r-process nucleosynthesis and can be seen as a kilonova — an optical emission of peak luminosity $\sim 10^{41}$ erg s $^{-1}$ lasting for a few weeks (see Roberts et al. 2011; Barnes & Kasen 2013; Bauswein et al. 2013; Kasen et al. 2013; Grossman et al. 2014; Wanajo et al. 2014; Barnes et al. 2016; Wu et al. 2017).

Second, during the merger, an accretion torus of $\sim 0.01 M_\odot$ forms around the BH with viscous time 0.1 s (Radice et al. 2016; Ruiz et al. 2016; Baiotti & Rezzolla 2017). Highly different masses of merging NSs are good for the formation of a massive disk, which can enhance jet power and aid its confinement. This accretion disk plays the most important part in our model. For a few seconds, the disk undergoes viscous spreading, produces powerful neutrino-driven winds, and exercises accretion onto the BH via the inner edge (presumably close to the innermost stable orbit), see Section 6.1. Interestingly, in the case of BH+NS merging, the neutrino heating mechanism (Eichler et al. 1989b; Birkl et al. 2007; Zalamea & Beloborodov 2011) can be the main source of the jet's energy (see Barkov & Pozanenko 2011). In the case of NS+NS merging, the mass of the accretion torus is relatively small ($< 10^{-2} M_\odot$), so the neutrino heating mechanism cannot be efficient on time scales of a few seconds.

At the same time, magnetic fields are amplified within the disk to $\sim 10^{15}$ G (Rezzolla et al. 2011) due to the development of MRI and the presence of the velocity shear. As the matter is accreted onto the BH, the BH accumulates magnetic flux. Accumulation of the magnetic flux leads to a delay for the jet to switch-on. At the same time, baryons slide off into the BH along magnetic field lines, leaving polar regions with low density. This creates conditions favorable for the operation of the Blandford–Znajek (BZ) mechanism (Blandford & Znajek 1977; Komissarov & Barkov 2009).

The BZ mechanism – production of EM outflows from the magnetic field supplied by the disk – also requires the presence of the external medium to produce jets (collimated outflows). It is the heavy baryonic wind from the disk that provides the required collimating surrounding. Importantly, the disk wind has only limited spatial extent – propagating with a velocity of $\sim 0.1c$ for about a few seconds it reaches out only to a few $\times 10^9$ cm. Outside of the wind, the surrounding is very clean.

The BZ jet propagates through a dense wind with mildly relativistic velocity (Section 6.3). At the same time, the jet is mildly dissipative (Section 4.1; and thus highly optically thick). In a few seconds, the head of the EM jet reaches the edge of the wind. During the breakout, the head part of the jet expands with highly relativistic velocities in the direction of jet propagation and moderately relativistic velocities to the sides. Sudden expansion leads to pair annihilation and the production of gamma-ray emission in a manner similar to conventional models of GRBs (Section 4.1). This is the prompt GRB.

After the jet breaks out from the wind, a rarefaction wave propagating toward the BH leads to the acceleration of the jet, which loses internal causal contact and propagates nearly ballistically (Figure 7). Since the jet emission is highly debeamed, the jet becomes unobservable. The wind emission shocked by the breaking-out jet produces the soft tail (Figure 7). A similar model for the formation of the first hard gamma-ray pulse was independently suggested in the paper by Gottlieb et al. (2017). This paper focuses on the effects of the jet breakout, both hydrodynamic and radiation processes.

4.1. *Jet Breakout – Prompt Hard GRB*

The BZ mechanism of jet launching requires clean plasma – there should be little mass loading and magnetic dissipation close to the source. This is indeed expected if the flow originates on field lines that penetrate the BH. It is expected that a jet launched by the BH is highly magnetized, $\sigma \gg 1$. Importantly, the confined jet with $\sigma \gg 1$ that propagates with non-relativistic velocity must necessarily be dissipative (Lyutikov 2006). Briefly, the magnetic flux and energy are supplied to the inflating bubble by a rate that cannot be accommodated within the bubble (this problem is also known as the σ-problem in pulsar winds; Rees & Gunn 1974; Kennel & Coroniti 1984). If dissipation becomes important, it will destroy a significant fraction of the magnetic energy and most importantly the toroidal flux will be eliminated. Latest 3D numerical simulations of pulsar wind nebulae indeed demonstrate that magnetic flux (and some magnetic energy) are dissipated within non-relativistically expanding cavities, thus resolving the σ-problem (Porth et al. 2013, 2014). A considerable fraction of the magnetic energy that has been produced before the jet breakout is dissipated.

At the time of the jet breakout its magnetization is not very high. At the breakout, the highly over-pressured jet loses both radial and lateral confinement. At this point, the jet dynamics changes in two important ways. First, the leading part of the jet expands nearly spherically, within a solid angle $\sim 2\pi$, with large Lorentz factors (see Lyutikov 2010; Lyutikov & Hadden 2012, for discussions of breakout dynamics in relativistic magnetized outflows; also, in Appendix D, we construct a simple model of a breakout of a magnetically dominated jet – the "force-free magnetic bomb"); the dynamics of non-magnetized relativistic breakout flows was considered by Johnson & McKee (1971); Nakar & Sari (2012); for discussions of breakout dynamics in core collapse supernovae, see, *e.g.* Weaver (1976); Tan et al. (2001); Ensman & Burrows (1992). At this point, the dynamics of pair-loaded magnetized outflows will resemble the conventional picture of magnetized GRB outflows (see, *e.g.* early discussion by Lyutikov & Usov 2000; Beloborodov 2017).

We suggest that this nearly spherical, highly relativistic outflow produces the prompt GRB spike. As the optically thick jet breaks out from the confining disk wind, the pair density falls out of equilibrium. Comptonization with the mildly optically thick region produces the observed GRB emission, similar to the photospheric emission in conventional GRB outflow (Beloborodov 2010; Beloborodov & Mészáros 2017). The emission is expected to peak at energies $\sim \Gamma \epsilon_{\rm ph} \geq 400$ keV, where $\epsilon_{\rm ph} \sim 20$ keV is the photospheric temperature in relativistic outflows (Paczynski 1986b) and $\Gamma \geq 25$ is the bulk Lorentz factor, see Eq. (1). Relativistic hydro-

dynamical simulations and calculation of jet brightness from a viewing angle can be found in Lazzati et al. (2017).

Second, the bulk of the jet accelerates along the jet axis – there is no more wind material to plow through. As the bulk of the jet accelerates to $\Gamma \gg 1$ (see (1)), its propagation becomes nearly ballistic.

5. OUTFLOW PARAMETERS INFERRED FROM OBSERVATIONAL CONSTRAINTS

5.1. *Lorentz Factor for the Prompt Spike*

For the hard prompt emission, using the total fluence of 2.3×10^{-7}erg cm^{-2}, the total energetics estimates to $\sim 4.9 \times 10^{46}$ erg, with peak power $\sim 10^{47}$ erg s^{-1}. The corresponding compactness parameter is large

$$l_c = \frac{L_\gamma \sigma_T \xi}{m_e c^4 t} = 3 \times 10^8 \xi t_{-0.3}^{-1}, \quad (1)$$

here ξ is the fraction of photons above the pair production threshold. Since the optical depth to pair production is $\propto l_c/\Gamma^6$ (*e.g.* Goodman 1986; Lithwick & Sari 2001), it is required that the flow producing the prompt burst accelerates to

$$\Gamma_{\rm j,min} = \left(\frac{\sigma_{\rm T} L_{\rm ht} \xi}{m_{\rm e} c^4 t} \right)^{1/6} \approx 25 \xi^{1/6}, \quad (2)$$

unfortunately, we have no information about the number of high-energy photons and our estimation Equation (2) can be significantly reduced. This in turn requires the emitting jet to be sufficiently clean (lacks baryons). This is an important constraint since the neutron-rich environment is expected to pollute the jet (Derishev et al. 1999; Beloborodov 2003).

5.2. *Opening Angle of the Jet from the Soft Gamma-Ray Component*

Properties of the soft thermal emission can be used to infer the geometrical properties of the outflow. In our model, the soft gamma-ray component originates from the wind material shocked by the jet and thus should have a physical size of the order of the jet radius at the moment of breakout. The total (thermal) luminosity of the second soft component is $L_{\rm ee} = 1.3 \times 10^{46}$ erg s^{-1}. Thus, the emitting area is

$$S = \frac{L_{\rm ee}}{\sigma_{SB} T_{\rm ee}^4} = 1.1 \times 10^{18} {\rm cm}^2 \quad (3)$$

and the radius of emitting region $r_{\rm S}$ is

$$r_{\rm S} = \sqrt{\frac{S}{\pi}} = 6 \times 10^8 {\rm cm}. \quad (4)$$

If the wind from the torus propagates with velocity $v_{\rm w} \approx 0.1c$ (see Barkov & Baushev 2011), then in 2.4 s it would expand to $r_{\rm w} \approx 7 \times 10^9$ cm. Thus, the jet opening angle is

$$\theta_{\rm j} = \frac{r_{\rm S}}{r_{\rm w}} \approx 0.08. \quad (5)$$

This value agrees well with results of GRMHD simulations (see Barkov 2008; Barkov & Baushev 2011; Kathirgamaraju et al. 2017).

5.3. *Magnetic Field at the Source*

As the jet breaks out from the wind, the quasispherical expansion of the jet material will form a fireball that resembles the pair-loaded fireball discussed earlier in the literature (Paczynski 1990; Rees & Mészáros 2005). A fraction $1/\eta_{\rm em} \ll 1$ of the energy stored in the wind prior to the jet-break will be radiated ($\eta_{\rm em}$ depends on parameters of outflow like the energy injection rate, magnetization, and baryonic loading (*e.g.* Lyutikov & Usov 2000).

We can relate the observed flux in the first/hard peak to the jet head energy density as

$$u_{\rm em} = \eta_{\rm em} \frac{4 L_{\rm peak}}{Sc}. \quad (6)$$

This can be used to estimate the equipartition magnetic field $B_{\rm eq}$ in the jet:

$$B_{\rm eq} = \frac{\sqrt{8\pi u_{\rm em}}}{\sqrt{3}} \approx 3 \times 10^{10} \eta_{\rm em,1}^{1/2} \ {\rm G}. \quad (7)$$

If originating from a BH with the surface field $B_{\rm BH}$, the magnetic field at the emission site is

$$B_{\rm eq} = B_{BH} \left(\frac{r_{\rm g}}{R_{\rm LC}} \right)^2 \frac{R_{\rm LC}}{r_{\rm S}}, \quad (8)$$

where $r_{\rm g}$ is BH Kerr radius, $R_{\rm C} \sim 4 r_{\rm g}/a_{\rm BH}$ is the light cylinder radius, and $a_{\rm BH}$ is the Kerr parameter. (Scaling is different from the NS case, here it is $R_{\rm LC}^2$ not $R_{\rm LC}^4$.)

Thus, the magnetic field on the surface of the BH can be estimated as

$$B_{\rm BH} \sim \frac{4}{a_{\rm BH}} \frac{r_{\rm S}}{r_{\rm g}} B_{\rm eq} \sim 2 \times 10^{14} \eta_{\rm em,1}^{1/2} a_{\rm BH,-0.2}^{-1} \ {\rm G}, \quad (9)$$

where we scaled the Kerr parameter to 0.7. These fields are higher, by about one or two orders of magnitude than is expected from surface magnetic fields of merging neutron stars, indicating that a dynamo process was operational during or after the merger (either on the collapsing neutron star or in the surrounding torus).

Substituting magnetic field from Eq. (9) to the equation of jet power

$$L_{\rm BZ} \approx \frac{B_{\rm BH}^2 r_{\rm g}^2 c}{24} f_{\rm BH}(a_{\rm BH}), \quad (10)$$

here $0 \le f_{\rm BH}(a_{\rm BH}) < 1$ is a factor that depends on the BH spin parameter (see more details in Blandford & Znajek 1977; Barkov & Komissarov 2008b), we obtain expected power as

$$L_j \sim 7 \eta_{\rm em} L_{\rm peak} \sim 10^{49} \eta_{\rm em,1} \ {\rm erg \ s^{-1}}. \quad (11)$$

To reiterate, Equation (11) related the power $L_{\rm ee}$ of the hard gamma-ray emission to the power of the BZ jet L_j. The estimate (11) compares favorably to the estimate of the jet power derived from modeling the evolution of the accretion torus, Equation (17), conversion parameter $\eta_{\rm em} \approx 10$, which corresponds to a jet power on of 10^{49} erg s^{-1} (see Paczynski 1990).

6. THE MODEL

6.1. *Evolution of the Accretion Disk*

As matter is accreted from the torus onto the BH, magnetic flux is accumulated on the BH. This triggers the BZ mechanism. It is expected that the value of the magnetic field that can be accumulated on the BH, and thus the jet power, depend on the accretion rate. Let us next estimate the maximal luminosity of a magnetically driven jet.

The accretion rate from the disk is $\dot{M}_d = 1.6M_{\rm d}/t_{\rm vis}$ (Shakura & Sunyaev 1973; Metzger et al. 2008a). Wind from the disk surface can significantly reduce accretion rate at the inner parts of the disk. Using the model of Blandford & Begelman (1999) and following Metzger et al. (2008a), the accretion rate onto the BH can be calculated as

$$\frac{dM_{\rm BH}}{dt} = \frac{1.6M_{\rm d}}{t_{\rm vis}} \left(\frac{r_{\rm ISCO}}{r_{\rm d}}\right)^p \left(\frac{(2p+1)t_{\rm vis}}{(2p+1)t_{\rm vis}+4.8t}\right)^{\frac{4(p+1)}{3}}, \quad (12)$$

here $0 < p < 1$ is a non-dimensional parameter that describes wind intensity,

$$r_{\rm d} = \left(\alpha_{\rm ss}^2 h_{\rm d}^4 G M_{\rm BH} t^2\right)^{1/3}, \quad (13)$$

here $h_{\rm d} = H/R$ is the relative thickness of the disk and $\alpha_{\rm ss}$ is the non-dimensional viscous parameter. The radius of the innermost stable circular orbit (ISCO) is

$$r_{\rm ISCO} = \frac{GM_{\rm BH} f(a_{\rm BH})}{c^2}, \quad (14)$$

here $1 < f(a_{\rm BH}) < 6$ is the non-dimensional radius of the last marginally stable orbit (Bardeen et al. 1972), which is a function of the BH spin parameter "$a_{\rm BH}$".

The accretion rate onto BH is

$$\frac{dM_{\rm BH}}{dt} = \frac{0.16(2p+1)^{\frac{4(p+1)}{3}} f(a_{\rm BH})^p M_{\rm d,-2} M_{\rm BH,0.5}^{\frac{2p}{3}} t_{\rm vis,-1}^{\frac{(2p+1)}{3}}}{60^p h_{\rm d,-0.5}^{\frac{4p}{3}} \alpha_{\rm ss,-1}^{\frac{2p}{3}} ((2p+1)t_{\rm vis,-1}+48t)^{\frac{4(p+1)}{3}}} \quad (15)$$

For the typical parameters of the NS+NS mergers (see Section 4), if we assume a conservative value of $p = 1/2$, the Equation (15) takes the form of

$$\frac{dM_{\rm BH}}{dt} = 0.02 \frac{f(a_{\rm BH})^{1/2} M_{\rm d,-2} M_{\rm BH,0.5}^{1/3} t_{\rm vis,-1}^{2/3}}{h_{\rm d,-0.5}^{2/3} \alpha_{\rm ss,-1}^{1/3} (t_{\rm vis,-1}+24t)^2} \quad M_\odot \ {\rm s}^{-1}. \quad (16)$$

The maximal jet power can be $L_{\rm BZ} = C(a_{\rm BH})\dot{M}_{\rm BH}c^2$, here $C(a_{\rm BH})$ is the efficiency of the accretion coefficient, $0 < C(a_{\rm BH}) <$ few (see, e.g., Komissarov & Barkov 2010; McKinney et al. 2012), which can be combined with factor $f(a_{\rm BH})$ and, for a wide range of BH spin parameter ($a_{\rm BH} > 0.3$), we obtain a simple approximation formula $C(a_{\rm BH})f(a_{\rm BH})^{1/2} \approx a_{\rm BH}^{2.4}$. If we adopt $a_{\rm BH} \approx 0.7$, we can estimate jet power as

$$L_{\rm BZ} \sim 10^{49} M_{\rm d,-2} M_{\rm BH,0.5}^{1/3} t_{\rm vis,-1}^{2/3} t_{0.3}^{-2} \quad {\rm erg \ s^{-1}}. \quad (17)$$

This equation is valid in the case $t \gg 0.4t_{\rm vis}$. So this electromagnetic luminosity corresponds to the strength of the magnetic field near the horizon of order (Blandford & Znajek 1977; Barkov & Komissarov 2008b)

$$B_{\rm BH} \approx \left(\frac{24L_{\rm BZ}}{r_{\rm g}^2 c}\right)^{1/2} \sim 2\times 10^{14} \quad {\rm G}. \quad (18)$$

This value, inferred from modeling the accretion torus, compares well with the one inferred from the soft X-ray component (Equation (9)).

6.2. *Optically Thick Pair-loaded Wind from the Disk*

The wind originates in a very optically thick and hot disk with $T \sim 1$ MeV. The optical thickness of the disk itself near the BH can be estimated from Equation (16) $\tau_{\rm d} \sim 3\times 10^{11} t^{-2}$. The wind is very optically thick, even without pair creation the expected optical depth to Thomson scattering is $\tau_T \gg 1$,

$$\tau_T \approx \frac{\sigma_T M_{\rm d}}{4m_p v_{\rm w}^2 t^2} \sim 5\times 10^{10} M_{\rm d,-2} v_{\rm ex,-1}^{-2} t_{0.3}^{-2}, \quad (19)$$

here we assume uniform density of the disk wind $\rho_{\rm w} = M_{\rm d}/4r_{\rm w}^3$. This result depends on the wind parameter p, which is neglected here. A large number of electron-positron pairs will be created near the disk. However, the $e^\pm$ pairs do not affect wind dynamics since baryon density exceeds the pair density by many orders of magnitude,

$$\frac{\rho_{\rm w}}{m_e n_\pm} = \frac{\sqrt{\pi/2}}{4} \frac{e^{r/(r_0\theta_{T,0})}}{m_e v_{\rm w} r^{1/2} r_0^{3/2} \theta_{T,0}^{3/2}} \gg 1$$

$$n_\pm \lambda_C^3 = \frac{\sqrt{2}}{\pi^{3/2}} e^{-\frac{1}{\theta_T}} \theta_T^{3/2}, \quad (20)$$

where $\lambda_C = \hbar/(m_e c)$ is the electron Compton length and we assumed the wind temperature is $T = T_0(r_0/r)$, normalized $\theta_T = T/m_e c^2$ (and similar for T_0) and used the equilibrium thermal pair density $n_\pm$ (Lightman 1982; Svensson 1982).

The wind will not produce any appreciable EM signatures due to steep adiabatic cooling. It is expected that the decay of radioactive elements contributes to wind heating, which together with far-flung tidal tails produce the kilonova emission (Li & Paczyński 1998; Metzger et al. 2010).

6.3. *Jet Propagation within the Wind*

Next, we consider the propagation of the BZ jet through the disk-generated wind. Since it takes time to accumulate the magnetic flux on the BH and to trigger the BZ mechanism, the jet will propagate through the pre-existing wind. Let the wind have constant properties (we neglect the fact that at early times the wind has higher $\dot{M}$; we might expect that this will be partially compensated by the initially higher $v_{\rm w}$). Consider a jet of power L_j that is confined within a solid angle $\Delta\Omega \approx \pi\theta^2$. The head of the jet located at r_h propagates with speed $v_{\rm jh}$ and according to (in the Kompaneets approximation, Kompaneets 1960)

$$P_{\rm jh} = \frac{L_j}{\pi\theta^2 r_h^2 c} = \rho_{\rm w}(v_{\rm jh} - v_{\rm w})^2. \quad (21)$$

where $P_{\rm jh}$ is the pressure created by the jet. Let us assume that the disk provides an outflow

$$\dot{M}_{\rm w,disk} = 4\pi v_{\rm w} \rho_{\rm w} r^2. \quad (22)$$

Using wind density from (22), the jet head propagates according to (see Bromberg et al. 2011)

$$v_{\rm jh} = v_{\rm w} + \sqrt{\frac{4L_j v_{\rm w}}{\theta^2 \dot{M}_{\rm w,disk} c}} \tag{23}$$

or

$$v_{\rm jh} = v_{\rm w} + 5\times10^9 L_{j,49}^{1/2} v_{\rm w,-1}^{1/2} \dot{M}_{\rm w,disk,-2}^{-1/2} {\rm cm\ s^{-1}}. \tag{24}$$

Thus, if the jet propagates with nearly constant velocity, then the jet propagation time is

$$t_{\rm jb} = \frac{v_{\rm w} t}{v_{\rm jh}} \sim \frac{t_{\rm delay}}{3}, \tag{25}$$

at the second half of this equation, we assume $v_{\rm w} = 0.1c = 3\times10^9$ cm s^{-1} and $v_{\rm jh} = 5\times10^9$ cm s^{-1} $\approx 2v_{\rm w}$. Moreover, if we again assume $v_{\rm w} = 0.1c$, this delay time is in good agreement with results of statistical analysis of short GRBs (Moharana & Piran 2017). Importantly, the head propagates within the wind with non-relativistic velocity.

If the speed of jet's head shock in the wind rest frame $v_{\rm s} = v_{\rm jh} - v_{\rm w} \geq v_{\rm w}$ is less than the wind speed, then the jet cocoon would have an approximately spherical shape in the expanding disk wind. And, in this case, after the shock breakout the head shock is not intense and could not form relativistic outflow and form a sufficiently large impact region at the boundary of the wind with the radius of $r_{\rm s} \sim r_{\rm w}$. So, comparing $v_{\rm s}$ and $v_{\rm w}$ from Equations (23) and (5), we can derive a restriction on the jet power as

$$L_j \geq \frac{S\dot{M}_{\rm w,disk} c}{4\pi v_{\rm w} t_{\rm delay}^2} \sim 3\times10^{48} \dot{M}_{\rm w,disk,-2} v_{w,-1}^{-1} \ {\rm erg\ s^{-1}}. \tag{26}$$

6.4. *Jet Lorentz Factor and Its Dynamics*

Let us estimate the Lorentz factor of the magnetically driven jet before the breakout from the wind. Magnetically driven jets can be accelerated up to very high Lorentz factors in the linear regime (Beskin & Nokhrina 2006; Barkov & Komissarov 2008a; Komissarov et al. 2009). In the case of the parabolic shape of the jet, we can estimate the jet Lorentz factor on the border expanding envelop as $\Gamma_{\rm j} = (r_{\rm S}/r_{\rm lc})^{1/2}$, here the cylindrical radius of the jet $r_{\rm S} = 6\times10^8$ cm and light cylinder radius $r_{\rm lc}$. In a case of fast spinning BH, $r_{\rm lc} = 4r_{\rm g}/a_{\rm BH} \approx 2\times10^6$ cm, for model parameters adopted in Section 4 this corresponds to $\Gamma_{\rm j} \approx 17$. We can treat this value as the minimal Lorentz factor of the jet. After the breakout, the jet can have additional boosting due to the formation of a strong rarefaction wave on its outer border (see Komissarov et al. 2010; Tchekhovskoy et al. 2010; Lyutikov 2011a; Kathirgamaraju et al. 2017). The additional opening angle, which is formed by sideways jet expansion, can be estimated as $\Delta\theta \approx 1/\Gamma_{\rm j} \approx 0.06$ (Lyutikov et al. 2003). So, the total opening angle of the jet can be estimated as $\theta_{\rm tot} = \theta + \Delta\theta \approx 0.15$.

6.5. *The Second Thermal Peak*

We can estimate the properties of the shock-heated wind flow at the point of breakout. Before the breakout, the BZ jet drives a shock in the wind. This shock is strongly radiation-dominated, as we demonstrate next (see Katz et al. 2010; Ito et al. 2017, for a discussion of radiation-dominated shocks). Equating post-shock plasma energy density to that of radiation, a shock becomes radiation-dominated for the post-shock (ion) temperatures T_r that satisfies

$$T_r > \left(\frac{15n}{\pi^2}\right)^{1/3} \frac{c\hbar}{k}, \tag{27}$$

where n is the pre-shock number density, and k is the Boltzmann constant. From the condition $kT = m_p v_r^2$, the required shock velocity is then

$$v_r \geq \sqrt{\frac{\hbar c}{m_p}} \left(\frac{15n}{\pi^2}\right)^{1/6}. \tag{28}$$

Comparing this with the relative velocity of the jet head with respect to the wind, (23),

$$\frac{v_{\rm jh} - v_{\rm w}}{v_r} = \frac{2^{4/3}\pi^{1/2}}{15^{1/6}} \frac{m_{\rm p}^{2/3}}{c\hbar^{1/2}} \frac{L_j^{1/2} v_{\rm w} t^{1/3}}{\theta \dot{M}_{d,wind}^{2/3}} \tag{29}$$

or

$$\frac{v_{\rm jh} - v_{\rm w}}{v_r} = 70 \frac{L_{j,49}^{1/2} v_{\rm w,-1} t_{0.3}^{1/3}}{\theta \dot{M}_{d,wind,-2}^{2/3}}. \tag{30}$$

The speed of the shock wave significantly exceeds the critical one, so we conclude that the jet-driven shock is radiatively dominated close to the breakout point.

In radiation-dominated shocks the post-shock temperature $T_{\rm s}$ is determined by the condition

$$\frac{4\sigma_{SB}}{c} T_{\rm s}^4 \sim \rho_{\rm w} (v_{\rm jh} - v_{\rm w})^2 = \frac{L_{\rm j}}{\pi (v_{\rm w} t\theta)^2 c}$$

$$T_{\rm s} = \frac{L_j^{1/4}}{(4\pi\sigma_{\rm SB})^{1/4} \sqrt{v_{\rm w} t\theta}}. \tag{31}$$

(Note that this estimate has a weak dependence on the properties of the jet (power and opening angle), is independent of the assumed mass loss rate of the disk, and only mildly dependent on the wind velocity.)

Substituting jet power from Equation (17), we get

$$T_{\rm s} = 40 \frac{M_{\rm d,-2}^{1/4}}{\theta_{-1}^{1/2} v_{\rm w,-1}^{1/2} t_{0.3}} \ {\rm keV}, \tag{32}$$

where time t is time of shock breakout. Estimate $T_{\rm s}$ is the upper limit since part of the energy incoming into the shock will be converted into bulk motion and into the production of pairs – these effects will reduce somewhat the post-shock temperature. At $t \sim$ a few seconds, and given our order-of-magnitude approach, this estimate is very close to the observed temperature of the second prompt peak.

6.6. *Estimate of the Viewing Angle*

In the present model, after the breakout, the collimated jet accelerates to highly relativistic velocities, and thus becomes highly debeamed and not observable. Let us estimate the constraints on the viewing angle.

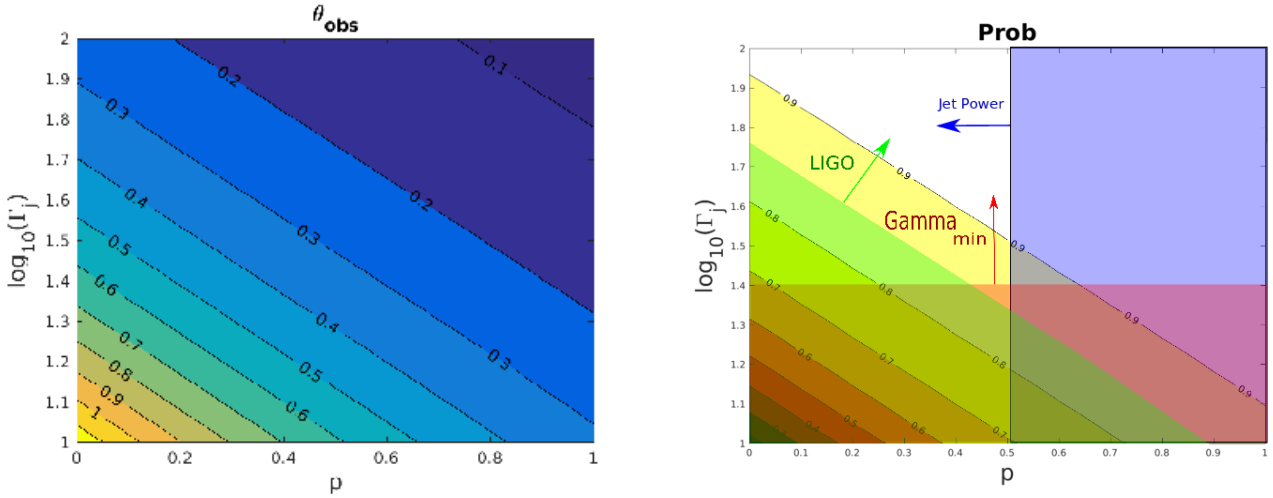

FIG. 8.— Observational angle (left) and probability to observe the transient (right) depends on wind parameter "p" and logarithm of the jet Lorentz factor $\Gamma_{\rm jet}$. In the right plot, we put limitation on the wind "p" parameter from Equations (26), (11), and (15) as purple area. The green area is following from LIGO observations.

The expected observed jet power of a relativistically boosted jet can be estimated as (see more details in Sikora et al. 1997)

$$L_{\rm obs} = \frac{\delta^3}{\Gamma_{\rm jet}} L_{\rm jet}, \tag{33}$$

here $\Gamma_{\rm jet}$ is the Lorentz factor of the jet, $\delta = 1/[\Gamma_{\rm jet}(1 - v\cos\theta/c)]$ is the Doppler factor of the jet, v is the velocity of the jet, θ is the angle between observer and jet axis, and $L_{\rm jet} = \chi L_{\rm BZ}$ is the electromagnetic jet luminosity with efficiency χ. In the case of small angles ($|1-\cos\theta| \ll 1$, but θ can be $\gg 1/\Gamma_{\rm jet}$), we can write $\Gamma_{\rm jet}/\delta = (\alpha^2 + 1)/2$ (Giannios et al. 2010; Aharonian et al. 2017), here $\alpha = \theta\Gamma_{\rm jet}$ and Equation (33) take the form

$$\alpha = \left[\left(\frac{8\Gamma_{\rm jet}^2 \chi L_{\rm BZ}}{L_{\rm obs}} \right)^{1/3} - 1 \right]^{1/2}. \tag{34}$$

In the case of large viewing angles ($\alpha \gg 1$), the Equation (34) can be writen as

$$\theta_{\rm side} = \left(\frac{8\chi L_{\rm BZ}}{\Gamma_{\rm jet}^4 L_{\rm obs}} \right)^{1/6}. \tag{35}$$

So, taking the jet opening angle from Section 6.4, the minimal viewing angle can be estimated as

$$\theta_{\rm obs} > \theta_{\rm tot} + \left(\frac{8\chi L_{\rm BZ}}{\Gamma_{\rm jet}^4 L_{\rm obs}} \right)^{1/6}. \tag{36}$$

Substituting parameters of the GRB 170817A to Equation (36), we can estimate the minimal viewing angle as

$$\theta_{\rm obs} > 0.15 + 0.3 \left(\frac{\chi M_{\rm d0,-2} M_{\rm BH,0.5}^{1/3} t_{\rm vis,-1}^{2/3}}{\Gamma_{\rm jet,15}^4 L_{\rm obs,47.2} \alpha_{\rm ss,-1} h_{\rm d,-0.5} t_{0.3}^2} \right)^{1/6}. \tag{37}$$

The probability to not observe such a burst is $Prob \approx 1 - \theta_{\rm obs}^2/2 \approx 1 - 0.1 \approx 0.9$. We should note that our limitation of observational angle is close to the value $\theta_{\rm GW} = 0.54$ obtained from BNS coalescence (LIGO Scientific Collaboration et al. 2017).

Combining Equations (15) and (34), we derive a minimal observational angle and probability to observe the transient and present them in Figure 8.

7. CONCLUSIONS

In this paper, we provide the results of the coordinated optical and radio search and optical observations of the LIGO/*Fermi* GBM event GW170817/GRB 170817A and propose a new theoretical model to explain the prompt gamma emission.

An optical transient of $\sim 19^m$ was detected by the Chilescope observatory. The properties of the optical transient match the kilonova activity (Smartt et al. 2017). We also provide upper limits on the possible short radio transient at 110 MHz associated with the GW170817/GRB 170817A at the trigger time.

We discuss the prompt gamma-ray emission, consisting of a hard gamma-ray pulse followed by a soft tail, each delayed by ~ 2 s with respect to the LIGO trigger. The appearance of the thermal component at the end of the burst is unusual for short GRBs. Both the hard pulse and the whole burst do not fit the Amati relation for short GRBs. This is especially true for the first hard pulse.

We then developed a theoretical model, which must explain (i) the delay between the LIGO and *Fermi* triggers; (ii) the two-component nature of the prompt emission; (iii) the absence of an afterglow.

Delay between LIGO and Fermi signals. The delay between the LIGO and the EM signals depends both on the delayed switching-on of the BZ-powered jet and the jet propagation through the dense expanding envelope (see Equation (25) and Gottlieb et al. 2018). The neutrino mechanism of jet launching is very sensitive to the disk temperature and should be more effective right after the disk formation; at this time, the accretion rate is also maximal. On the other hand, the BZ mechanism is less sensitive to accretion rate and needs sufficient magnetic flux accumulated on the BH, (see, e.g., Komissarov & Barkov 2009). Also, an operation of the BZ mechanism

requires magnetically dominated plasma - the cleaning of polar regions of the BH can take about 1 s (Barkov & Komissarov 2010). We suggest the observed delay results from both the delay of activation of the BZ jet and the jet propagation through expanding envelope.

Two components of prompt emission. We suggest in our model that the two components come from, first, highly relativistic, nearly isotropic breakout of a magnetized jet from the confining wind, and, second, from the wind material heated by the breaking-out jet. After activation of the BZ process, the jet head propagates through wind matter with subrelativistic velocity. The initially strongly magnetically dominated jet partially transfers its magnetic energy into internal energy, as discussed in Section 4.1. During the jet breakout from the confining wind, the jet expands quasi-isotropically (see Figure 6). The expanding matter accelerates up to the high Lorentz factor (see Equation (2)) at the radius of $r_{\rm ha} \approx \Gamma_{\rm j,min} r_{\rm S} \approx 10^{10}$ cm, where the cloud becomes transparent for radiation. The minimal variability time $\sim r_{\rm s}/c \sim 0.02$ s does not contradict the duration of the first hard pulse. The second soft gamma-ray component is formed by thermal emission of shocked stellar wind matter. This interpretation allows us to put self-consistent restrictions on the cylindrical radius of the jet $r_{\rm S} = 6 \times 10^8$ cm, power of the jet $L_{\rm jet} \sim 10^{49}$ erg s^{-1} and jet penetration time through the wind envelope. Also, we estimate jet power which can be supplied by the magnetically driven jet supported by the accretion disk with the wind (see Equations (26), (11), and (17)).

Absence of early afterglows. We suggest that the absence of the afterglow can be explained by the observer off-axis to the jet. After the jet breaks out, a standard jet acceleration will be recovered - the BZ flow accelerates to $\Gamma \geq 17$ at the edge of the wind and after that jet boosts its acceleration. Later, the jet becomes causally disconnected and propagates ballistically. This boost in acceleration will suppress the visibility of the BZ jet, and the corresponding forward shock. Importantly, the luminosity of an afterglow component of GRB 170817A is less by factors at least 30 in r-filter and 130 in J-filter than the afterglow of GRB 130603B at ∼11 hr after burst onset (see Figure 11).

ACKNOWLEDGMENTS

A.S.P., P.Yu.M., A.A.V., and E.D.M. are grateful to RFBR grants 17-02-01388 and 17-52-80139 for partial support. This work was supported by NSF grant AST-1306672, DoE grant DE-SC0016369, and NASA grant 80NSSC17K0757. We acknowledge the excellent help in obtaining Chilescope data provided by Sergei Pogrebisskiy and Ivan Rubtsov. We are grateful to the anonymous referee for the thorough reading of the article and for useful comments that contributed to the improvement of the article.

REFERENCES

Aharonian, F. A., Barkov, M. V., & Khangulyan, D. 2017, ApJ, 841, 61
Allam, S., Annis, J., Berger, E., & et al. 2017, GCN, 21530 LVC
Amati, L. 2010, arXiv:1002.2232
Arcavi, I., Howell, D. A., McCully, C., & et al. 2017, GCN, 21538 LVC
Baiotti, L., & Rezzolla, L. 2017, Reports on Progress in Physics, 80, 096901
Bardeen, J. M., Press, W. H., & Teukolsky, S. A. 1972, ApJ, 178, 347
Barkov, M. V. 2008, in American Institute of Physics Conference Series, Vol. 1054, American Institute of Physics Conference Series, ed. M. Axelsson, 79–85
Barkov, M. V., & Baushev, A. N. 2011, New Astr., 16, 46
Barkov, M. V., & Komissarov, S. S. 2008a, International Journal of Modern Physics D, 17, 1669
—. 2008b, MNRAS, 385, L28
—. 2010, MNRAS, 401, 1644
Barkov, M. V., & Pozanenko, A. S. 2011, MNRAS, 417, 2161
Barnes, J., & Kasen, D. 2013, ApJ, 775, 18
Barnes, J., Kasen, D., Wu, M.-R., & Martínez-Pinedo, G. 2016, ApJ, 829, 110
Bauswein, A., Goriely, S., & Janka, H.-T. 2013, ApJ, 773, 78
Beloborodov, A. M. 2003, ApJ, 588, 931
—. 2010, MNRAS, 407, 1033
—. 2017, ApJ, 838, 125
Beloborodov, A. M., & Mészáros, P. 2017, Space Sci. Rev., 207, 87
Beskin, V. S., & Nokhrina, E. E. 2006, MNRAS, 367, 375
Birkl, R., Aloy, M. A., Janka, H., & Müller, E. 2007, åp, 463, 51
Bisnovatyi-Kogan, G. S. 1970, AZh, 47, 813
Blandford, R. D., & Begelman, M. C. 1999, MNRAS, 303, L1
Blandford, R. D., & Znajek, R. L. 1977, MNRAS, 179, 433
Blinnikov, S. I., Novikov, I. D., Perevodchikova, T. V., & Polnarev, A. G. 1984, Pis ma Astronomicheskii Zhurnal, 10, 422
Bromberg, O., Nakar, E., Piran, T., & Sari, R. 2011, ApJ, 740, 100
Brown, T. M., Baliber, N., Bianco, F. B., & et al. 2013, PASP, 125, 1031
Cash, W. 1979, ApJ, 228, 939
Connaughton, V., Blackburn, L., Briggs, M. S., Broida, J., & Burns, E. 2017, GCN, 21506 LVC
Coulter, D. A., Kilpatrick, C. D., Siebert, M. R., Foley, R. J., Shappee, B. J., Drout, M. R., Simon, J. S., & Piro, A. L. 2017, GCN, 21529 LVC
Dalya, G., Frei, Z., Galgoczi, G., Raffai, P., & de Souza, R. S. 2016, VizieR Online Data Catalog, 7275
Derishev, E. V., Kocharovsky, V. V., & Kocharovsky, V. V. 1999, ApJ, 521, 640
Eichler, D., & Levinson, A. 2004, ApJ, 614, L13
Eichler, D., Livio, M., Piran, T., & Schramm, D. N. 1989a, Nature, 340, 126
—. 1989b, Nature, 340, 126
Ensman, L., & Burrows, A. 1992, ApJ, 393, 742
Fenimore, E. E., in 't Zand, J. J. M., Norris, J. P., Bonnell, J. T., & Nemiroff, R. J. 1995, ApJ, 448, L101
Giannios, D., Uzdensky, D. A., & Begelman, M. C. 2010, MNRAS, 402, 1649
Goldstein, A., Veres, P., Burns, E., & et al. 2017a, ApJ, 848, L14
Goldstein, A., Veres, P., von Kienlin, A., Blackburn, L., & Briggs, M. S. 2017b, GCN, 21528 LVC
Goodman, J. 1986, ApJ, 308, L47
Gottlieb, O., Nakar, E., & Piran, T. 2018, MNRAS, 473, 576
Gottlieb, O., Nakar, E., Piran, T., & Hotokezaka, K. 2017, ArXiv :astro-ph/1710.05896
Gralla, S. E., & Jacobson, T. 2014, MNRAS, 445, 2500
Grossman, D., Korobkin, O., Rosswog, S., & Piran, T. 2014, MNRAS, 439, 757
Gruber, D., Goldstein, A., Weller von Ahlefeld, V., & et al. 2014, ApJS, 211, 12
Gruzinov, A. 1999, ArXiv:9902288
Ito, H., Levinson, A., Stern, B. E., & Nagataki, S. 2017, ArXiv e-prints
Johnson, M. H., & McKee, C. F. 1971, Phys. Rev. D, 3, 858
Jones, D. H., Read, M. A., Saunders, W., & et al. 2009, MNRAS, 399, 683
Kasen, D., Badnell, N. R., & Barnes, J. 2013, ApJ, 774, 25
Kathirgamaraju, A., Barniol Duran, R., & Giannios, D. 2017, arXiv:1708.07488
Katz, B., Budnik, R., & Waxman, E. 2010, ApJ, 716, 781
Kennel, C. F., & Coroniti, F. V. 1984, ApJ, 283, 694
Komissarov, S. S. 2011, MNRAS, 418, L94
Komissarov, S. S., & Barkov, M. V. 2009, MNRAS, 397, 1153
—. 2010, MNRAS, 402, L25
Komissarov, S. S., Vlahakis, N., & Königl, A. 2010, MNRAS, 407, 17
Komissarov, S. S., Vlahakis, N., Königl, A., & Barkov, M. V. 2009, MNRAS, 394, 1182
Kompaneets, A. S. 1957, Sov. Phys. JETP, 4, 730
—. 1960, Soviet Physics Doklady, 5, 46

Lazzati, D., López-Cámara, D., Cantiello, M., Morsony, B. J., Perna, R., & Workman, J. C. 2017, ApJ, 848, L6
LeBlanc, J. M., & Wilson, J. R. 1970, ApJ, 161, 541
Levinson, A., & Eichler, D. 2005, ApJ, 629, L13
Li, L.-X., & Paczyński, B. 1998, ApJ, 507, L59
Lightman, A. P. 1982, ApJ, 253, 842
LIGO Scientific Collaboration, & Virgo Collaboration. 2017, GCN, 21505 LVC
LIGO Scientific Collaboration, VIRGO Collaboration, Partner Astronomy Groups, Abbott, & et al. 2017, ApJ, 848, L13
Lipunov, V., Kornilov, V., Gorbovskoy, E., & et al. 2010, Advances in Astronomy, 2010, 349171
Lipunov, V. M., Gorbovskoy, E., Kornilov, V. G., & et al. 2017, GCN, 21546 LVC
Lithwick, Y., & Sari, R. 2001, ApJ, 555, 540
Lyutikov, M. 2006, New Journal of Physics, 8, 119
—. 2010, Phys. Rev. E, 82, 056305
—. 2011a, MNRAS, 411, 422
—. 2011b, Phys. Rev. D, 83, 124035
—. 2011c, Phys. Rev. D, 83, 064001
Lyutikov, M., & Hadden, S. 2012, Phys. Rev. E, 85, 026401
Lyutikov, M., Pariev, V. I., & Blandford, R. D. 2003, ApJ, 597, 998
Lyutikov, M., & Usov, V. V. 2000, ApJ, 543, L129
McKinney, J. C., Tchekhovskoy, A., & Blandford, R. D. 2012, MNRAS, 423, 3083
Metzger, B. D., Martínez-Pinedo, G., Darbha, S., & et al. 2010, MNRAS, 406, 2650
Metzger, B. D., Piro, A. L., & Quataert, E. 2008a, MNRAS, 390, 781
Metzger, B. D., Quataert, E., & Thompson, T. A. 2008b, MNRAS, 385, 1455
Minaev, P. Yu., & Pozanenko, A. S. 2017, Astronomy Letters, 43, 1
Minaev, P. Yu., Pozanenko, A. S., & Loznikov, V. M. 2010a, Astronomy Letters, 36, 707
—. 2010b, Astrophysical Bulletin, 65, 326
Minaev, P. Yu., Pozanenko, A. S., Molkov, S. V., & Grebenev, S. A. 2014, Astronomy Letters, 40, 235
Moharana, R., & Piran, T. 2017, MNRAS, 472, L55
Moiseenko, S. G., Bisnovatyi-Kogan, G. S., & Ardeljan, N. V. 2006, MNRAS, 370, 501
Nakar, E., & Sari, R. 2012, ApJ, 747, 88
Paczynski, B. 1986a, ApJ, 308, L43
—. 1986b, ApJ, 308, L43
—. 1990, ApJ, 363, 218
Porth, O., Komissarov, S. S., & Keppens, R. 2013, MNRAS, 431, L48
—. 2014, MNRAS, 438, 278
Pozanenko, A., Mazaeva, E., Volnova, A., Minaev, P., & Krugov, M. 2017a, LVC GRB Coordinates Network, 21618
Pozanenko, A., Volnova, A., Mazaeva, E., Minaev, P., & Krugov, M. 2017b, GCN, 21635 LVC
Pozanenko, A., Volnova, A., Mazaeva, E., Minaev, P., Moskvitin, A., & Krugov, M. 2017c, GCN, 21898 LVC
Pozanenko, A., Volnova, A., Minaev, P., & Krugov, M. 2017d, GCN, 21644 LVC
Qin, Y.-P., & Chen, Z.-F. 2013, MNRAS, 430, 163
Radice, D., Galeazzi, F., Lippuner, J., Roberts, L. F., Ott, C. D., & Rezzolla, L. 2016, MNRAS, 460, 3255
Rees, M. J., & Gunn, J. E. 1974, MNRAS, 167, 1
Rees, M. J., & Mészáros, P. 2005, The Astrophysical Journal, 628, 847
Rezzolla, L., Giacomazzo, B., Baiotti, L., Granot, J., Kouveliotou, C., & Aloy, M. A. 2011, ApJ, 732, L6
Roberts, L. F., Kasen, D., Lee, W. H., & Ramirez-Ruiz, E. 2011, ApJ, 736, L21
Ruiz, M., Lang, R. N., Paschalidis, V., & Shapiro, S. L. 2016, ApJ, 824, L6
Samodurov, V., Pozanenko, A. S., Rodin, E. A., & et al. 2017, in Data Analytics and Management in Data Intensive Domains. DAMDID/RCDL 2016. Communications in Computer and Information Science, Vol. 706, Communications in Computer and Information Science, ed. K. S. Kalinichenko L.
Savchenko, V., Ferrigno, C., Kuulkers, E., & et al. 2017a, ApJ, 848, L15
Savchenko, V., Mereghetti, S., Ferrigno, C., Kuulkers, E., & Bazzano, A. 2017b, GCN, 21507 LVC
Schlafly, E. F., & Finkbeiner, D. P. 2011, ApJ, 737, 103
Shakura, N. I., & Sunyaev, R. A. 1973, A&A, 24, 337
Sikora, M., Madejski, G., Moderski, R., & Poutanen, J. 1997, ApJ, 484, 108
Smartt, S. J., Chen, T.-W., Jerkstrand, A., & et al. 2017, Nature, 551, 75
Svensson, R. 1982, ApJ, 258, 335
Svinkin, D. S., Frederiks, D. D., Aptekar, R. L., & et al. 2016, ApJS, 224, 10
Tan, J. C., Matzner, C. D., & McKee, C. F. 2001, ApJ, 551, 946
Tanvir, N. R., & Levan, A. J. 2017, GCN, 21544 LVC
Tanvir, N. R., Levan, A. J., Fruchter, A. S., Hjorth, J., Hounsell, R. A., Wiersema, K., & Tunnicliffe, R. L. 2013, Nature, 500, 547
Tanvir, N. R., Levan, A. J., González-Fernández, C., & et al. 2017, ApJ, 848, L27
Tchekhovskoy, A., Narayan, R., & McKinney, J. C. 2010, New Astr., 15, 749
Usov, V. V. 1992, Nature, 357, 472
Viganò, D., & Mereghetti, S. 2009, in The Extreme Sky: Sampling the Universe above 10 keV
Villar, V. A., Guillochon, J., Berger, E., & et al. 2017, arXiv:1710.11576
von Kienlin, A., Beckmann, V., Rau, A., & et al. 2003, A&A, 411, L299
von Kienlin, A., Meegan, C., & Goldstein, A. 2017, LVC GRB Coordinates Network, 21520
von Kienlin, A., Meegan, C. A., Paciesas, W. S., & et al. 2014, ApJS, 211, 13
Wanajo, S., Sekiguchi, Y., Nishimura, N., Kiuchi, K., Kyutoku, K., & Shibata, M. 2014, ApJ, 789, L39
Weaver, T. A. 1976, ApJS, 32, 233
Wu, M.-R., Tamborra, I., Just, O., & Janka, H.-T. 2017, ArXiv e-prints
Yang, S., Valenti, S., Sand, D., Tartaglia, L., Cappellaro, E., Reichart, D., Haislip, J., & Kouprianov, V. 2017, GCN, 21531 LVC
Zalamea, I., & Beloborodov, A. M. 2011, MNRAS, 410, 2302

APPENDIX

A. OPTICAL OBSERVATIONS OF CHILESCOPE OBSERVATORY

A.1. *The CHILESCOPE*

The CHILESCOPE[4] is a remote controlled commercial observatory located in the Chilean Andes (W 70.75 S 30.27) equipped with a 1 m Ritchey Chretien telescope (RC-1000) and two identical 50 cm fast Newton astrographs (Newtonian 1 ASA-500 and Newtonian 2).

Both Newtonians with $f/3.8$ are on "Z" equatorial mounts, both are equipped with 4K×4K FLI PROLINE 16803 CCD cameras with Astrodon Generation 2 E-Series Luminance filter [5], which is approximately equivalent to a clear light. The field of view is 67×67 arcminutes.

The 1-meter RC-1000 telescope is mounted on an alt-azimuth mount with direct drives on both axes and has a focal ratio $f/6.8$ with a reducer. The telescope is also equipped with a 4K×4K FLI PROLINE 16803 CCD camera with Astrodon Generation 2 E-Series Luminance filter. It effectively cuts off the wavelengths < 4000 Å and > 7100 Å, thus its transmission curve corresponds to a clear light. In the paper, we refer to this filter as Clear. The resulting field of view is 18.6×18.6 arcminutes. It also has a good thermal stabilization with the working temperature of -30°C.

[4] http://www.chilescope.com/

[5] https://www.cloudynights.com/uploads/monthly_09_2014/post-23216-0-17456300-1411330347.jpg

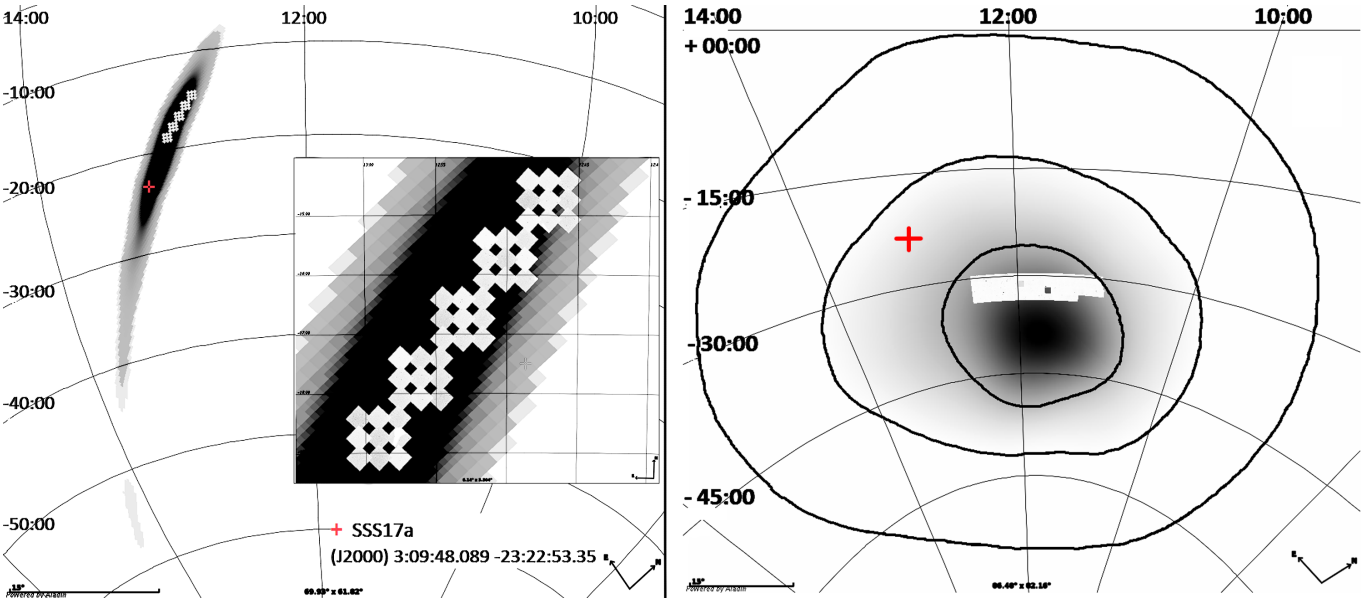

FIG. 9.— Mosaic observations of the RC-1000 telescope (left panel) and the ASA-500 telescope (right panel). The figure shows the LIGO/Virgo error box with partial coverage by the RC-1000 telescope observations (left panel). Observations of the RC-1000 telescope began 11.1 hr after the GW trigger. Coverage of ASA-500 telescope observations of the GBM/*Fermi* localization area of GRB 170817A is shown in the right panel. Localization area at 1, 2, and 3σ are shown by thick curves. Observations of the ASA-500 telescope began 10.6 hr after the GW trigger. The red cross is the position of the optical counterpart (R.A.(J2000)=03:09:48.089, Decl.(J2000)=-23:22:53.35).

A.2. *Observations of the RC-1000 telescope*

The RC-1000 telescope covered the central part of the LIGO/Virgo trigger G298048 error box (LIGO Scientific Collaboration & Virgo Collaboration 2017) with a typical limiting magnitude of 20^m at 60 s exposure in each frame. A total of 48 images were obtained. The coverage of the 1σ error box of G298048 is 14.4 %. The start time (UT) and the center coordinates of each frame are collected in Table 3. The optical counterpart candidate SSS17a was independently discovered by six teams (Allam et al. 2017; Arcavi et al. 2017; Coulter et al. 2017; Lipunov et al. 2017; Tanvir & Levan 2017; Yang et al. 2017) with the first announcement at 01:05 UT Auggust 18 (12.4 hr since GW trigger and 25.6 minutes after the end of RC-1000 telescope observations). The localization of SSS17a is out of the coverage in the first epoch of our observations. The covering map can be found in Figure 9, left panel.

A.3. *Observations the of ASA-500 telescope*

We also covered the northern part of the GBM/*Fermi* localization 1σ containment (statistical only, Connaughton et al. 2017) with several frames taken by the ASA-500 telescope in the Clear filter. The total coverage of the GBM 1σ localization area is about 16 % and contains 76 frames. The typical limiting magnitude of a single frame is $17\overset{\text{m}}{.}5$ at 60 s exposure. Date, start time of observations (UT), and center coordinates of each frame are collected in Tables 4 and 5. The covering map can be found in Figure 9, right panel.

A.4. *SSS17a observations*

We started to observe the optical counterpart of the GW170817 (LIGO Scientific Collaboration & Virgo Collaboration 2017) labeled SSS17a (Coulter et al. 2017) on 2017 August 19 at 23:30:33 UT taking several 180 s exposures in the Clear filter with the RC-1000 telescope of the CHILESCOPE observatory (Pozanenko et al. 2017b). We clearly detected the source strongly contaminated by the host galaxy NGC 4993 background. We continued our observations on 2017 August 20, 21, and 24, taking several 180 s exposures in each epoch (Pozanenko et al. 2017d,c). The weather conditions were satisfactory with a median seeing of 2 arcsec. The seeing was not good for the Chilean sky because the source was observed in the end of twilight when the atmosphere was not stable. The source was clearly detected in the stacked frames on August 20 and 21 but faded on August 24 below the detection limit over a host galaxy background. The optical transient SSS17a is shown in Figure 10. The log of our observations is listed in the Table 6.

A.5. *Data Reduction and Photometry*

All primary reduction of CCD images (bias and dark subtraction, flat-fielding) was performed using the CCDPROC task of the IRAF software package[6]. The flux of the source is strongly affected by the host galaxy contribution, so the strategy of direct image subtraction was decided. Since the source was not detected in the stacked frame of the last observational epoch (August 24), we chose this epoch as a template for the subtraction of the host galaxy. To align images of different observational epochs, we used the package ALIGN/IMAGE of ESO-MIDAS software[7] and

[6] `http://iraf.noao.edu/`

[7] `http://www.eso.org/sci/software/esomidas/`

TABLE 3
Observations of the RC-1000 telescope

UT Date	Time Since GW Trigger (days)	Center (R.A.)	Center (Decl.)
2017 Aug 17 23:44:31	0.46108	12 ^{h} 48 ^{m} 28^s.414	-14 °25 ′07.″037
2017 Aug 17 23:45:53	0.46203	12 ^{h} 47 ^{m} 05^s.895	-14 °25 ′04.″261
2017 Aug 17 23:47:16	0.46299	12 ^{h} 45 ^{m} 43^s.416	-14 °25 ′01.″827
2017 Aug 17 23:48:38	0.46394	12 ^{h} 48 ^{m} 28^s.594	-14 °45 ′01.″452
2017 Aug 17 23:50:00	0.46488	12 ^{h} 47 ^{m} 05^s.988	-14 °44 ′59.″153
2017 Aug 17 23:51:23	0.46584	12 ^{h} 45 ^{m} 43^s.329	-14 °44 ′57.″545
2017 Aug 17 23:52:45	0.46679	12 ^{h} 48 ^{m} 28^s.701	-15 °04 ′58.″286
2017 Aug 17 23:54:07	0.46774	12 ^{h} 47 ^{m} 05^s.854	-15 °04 ′58.″530
2017 Aug 17 23:55:30	0.46870	12 ^{h} 45 ^{m} 43^s.005	-15 °04 ′59.″031
2017 Aug 17 23:58:01	0.47045	12 ^{h} 51 ^{m} 28^s.799	-15 °25 ′03.″691
2017 Aug 17 23:59:23	0.47140	12 ^{h} 50 ^{m} 05^s.874	-15 °25 ′02.″099
2017 Aug 18 00:00:46	0.47236	12 ^{h} 48 ^{m} 42^s.901	-15 °25 ′00.″518
2017 Aug 18 00:02:17	0.47341	12 ^{h} 51 ^{m} 28^s.942	-15 °45 ′00.″766
2017 Aug 18 00:03:49	0.47448	12 ^{h} 50 ^{m} 05^s.842	-15 °44 ′59.″895
2017 Aug 18 00:05:22	0.47556	12 ^{h} 48 ^{m} 42^s.695	-15 °44 ′56.″860
2017 Aug 18 00:06:53	0.47661	12 ^{h} 51 ^{m} 28^s.907	-16 °04 ′59.″101
2017 Aug 18 00:08:15	0.47756	12 ^{h} 50 ^{m} 05^s.657	-16 °04 ′57.″618
2017 Aug 18 00:09:38	0.47852	12 ^{h} 48 ^{m} 42^s.360	-16 °04 ′57.″688
2017 Aug 18 00:13:16	0.48104	12 ^{h} 51 ^{m} 28^s.630	-15 °25 ′05.″288
2017 Aug 18 00:14:38	0.48199	12 ^{h} 50 ^{m} 05^s.706	-15 °25 ′02.″368
2017 Aug 18 00:17:15	0.48381	12 ^{h} 54 ^{m} 29^s.036	-16 °25 ′02.″125
2017 Aug 18 00:18:50	0.48491	12 ^{h} 54 ^{m} 29^s.003	-16 °25 ′03.″603
2017 Aug 18 00:20:21	0.48596	12 ^{h} 53 ^{m} 05^s.630	-16 °25 ′02.″356
2017 Aug 18 00:21:52	0.48701	12 ^{h} 51 ^{m} 42^s.259	-16 °25 ′00.″875
2017 Aug 18 00:23:22	0.48806	12 ^{h} 54 ^{m} 29^s.055	-16 °45 ′00.″484
2017 Aug 18 00:24:53	0.48911	12 ^{h} 53 ^{m} 05^s.560	-16 °44 ′58.″705
2017 Aug 18 00:26:26	0.49019	12 ^{h} 51 ^{m} 41^s.997	-16 °44 ′57.″424
2017 Aug 18 00:27:57	0.49124	12 ^{h} 54 ^{m} 29^s.024	-17 °04 ′59.″058
2017 Aug 18 00:29:20	0.49220	12 ^{h} 53 ^{m} 05^s.393	-17 °04 ′59.″049
2017 Aug 18 00:30:42	0.49315	12 ^{h} 51 ^{m} 41^s.709	-17 °04 ′58.″549
2017 Aug 18 00:34:03	0.49547	12 ^{h} 57 ^{m} 29^s.158	-17 °25 ′03.″586
2017 Aug 18 00:35:33	0.49652	12 ^{h} 56 ^{m} 05^s.408	-17 °25 ′02.″790
2017 Aug 18 00:37:04	0.49757	12 ^{h} 54 ^{m} 41^s.653	-17 °24 ′59.″856
2017 Aug 18 00:38:26	0.49852	12 ^{h} 57 ^{m} 29^s.218	-17 °45 ′01.″451
2017 Aug 18 00:39:49	0.49948	12 ^{h} 56 ^{m} 05^s.305	-17 °44 ′59.″001
2017 Aug 18 00:41:19	0.50052	12 ^{h} 54 ^{m} 41^s.310	-17 °44 ′57.″055
2017 Aug 18 00:42:50	0.50157	12 ^{h} 57 ^{m} 29^s.230	-18 °04 ′59.″511
2017 Aug 18 00:44:13	0.50253	12 ^{h} 56 ^{m} 05^s.075	-18 °04 ′58.″201
2017 Aug 18 00:45:35	0.50348	12 ^{h} 54 ^{m} 40^s.882	-18 °04 ′57.″991
2017 Aug 18 00:48:13	0.50531	13 ^{h} 00 ^{m} 29^s.457	-18 °25 ′01.″845
2017 Aug 18 00:49:43	0.50635	12 ^{h} 59 ^{m} 05^s.148	-18 °25 ′01.″236
2017 Aug 18 00:51:06	0.50731	12 ^{h} 57 ^{m} 40^s.809	-18 °24 ′59.″051
2017 Aug 18 00:52:28	0.50826	13 ^{h} 00 ^{m} 29^s.458	-18 °44 ′59.″417
2017 Aug 18 00:53:50	0.50921	12 ^{h} 59 ^{m} 04^s.993	-18 °44 ′57.″667
2017 Aug 18 00:55:23	0.51029	12 ^{h} 57 ^{m} 40^s.424	-18 °44 ′56.″776
2017 Aug 18 00:56:54	0.51134	13 ^{h} 00 ^{m} 29^s.415	-19 °04 ′57.″375
2017 Aug 18 00:58:25	0.51240	12 ^{h} 59 ^{m} 04^s.778	-19 °04 ′57.″208
2017 Aug 18 00:59:57	0.51346	12 ^{h} 57 ^{m} 40^s.097	-19 °04 ′55.″261

the `geomap` task of IRAF. The average image background was subtracted from all frames using median filter, and flux normalization for the image subtraction was performed using the MAGNITUDE/CIRCLE task of ESO-MIDAS.

The photometry of the source after the host subtraction was made with the PSF method using the DAOPHOT package from IRAF software. A rectangular area containing the host galaxy and the source SSS17a was replaced in the stacked background-subtracted frames with the host subtracted flux-normalized sub-images, made for each observational epoch. The reference PSF stars for each specific epoch were taken from the area outside of the host subtraction region.

TABLE 4
Observations of ASA-500 telescope

UT Date	Time Since GW Trigger (days)	Center (R.A.)	Center (Decl.)
2017 Aug 17 23:17:16	0.44215	12 ^{h} 30 ^{m} 15^s.598	-30 °12 ′47.″661
2017 Aug 17 23:18:42	0.44315	12 ^{h} 25 ^{m} 37^s.552	-30 °12 ′46.″982
2017 Aug 17 23:20:08	0.44414	12 ^{h} 20 ^{m} 59^s.825	-30 °12 ′51.″272
2017 Aug 17 23:21:34	0.44514	12 ^{h} 16 ^{m} 22^s.006	-30 °12 ′54.″690
2017 Aug 17 23:23:00	0.44613	12 ^{h} 11 ^{m} 44^s.220	-30 °12 ′56.″952
2017 Aug 17 23:24:26	0.44713	12 ^{h} 07 ^{m} 06^s.472	-30 °12 ′59.″341
2017 Aug 17 23:25:51	0.44811	12 ^{h} 02 ^{m} 28^s.537	-30 °13 ′04.″766
2017 Aug 17 23:27:08	0.44900	11 ^{h} 57 ^{m} 50^s.769	-30 °13 ′06.″317
2017 Aug 17 23:28:26	0.44991	11 ^{h} 53 ^{m} 12^s.785	-30 °13 ′12.″156
2017 Aug 17 23:29:51	0.45089	11 ^{h} 48 ^{m} 34^s.883	-30 °13 ′16.″196
2017 Aug 17 23:31:09	0.45179	11 ^{h} 43 ^{m} 56^s.993	-30 °13 ′19.″841
2017 Aug 17 23:32:26	0.45269	11 ^{h} 38 ^{m} 46^s.482	-31 °13 ′44.″353
2017 Aug 17 23:33:51	0.45367	11 ^{h} 34 ^{m} 41^s.269	-30 °13 ′27.″977
2017 Aug 17 23:35:09	0.45457	11 ^{h} 30 ^{m} 03^s.364	-30 °13 ′34.″495
2017 Aug 17 23:36:26	0.45546	11 ^{h} 25 ^{m} 25^s.436	-30 °13 ′37.″753
2017 Aug 17 23:37:51	0.45645	11 ^{h} 20 ^{m} 47^s.749	-30 °13 ′41.″649
2017 Aug 17 23:39:16	0.45743	11 ^{h} 16 ^{m} 09^s.869	-30 °13 ′48.″310
2017 Aug 17 23:40:34	0.45833	11 ^{h} 11 ^{m} 31^s.887	-30 °13 ′52.″435
2017 Aug 17 23:41:51	0.45922	11 ^{h} 06 ^{m} 54^s.122	-30 °13 ′57.″672
2017 Aug 17 23:43:16	0.46021	11 ^{h} 02 ^{m} 16^s.046	-30 °14 ′03.″015
2017 Aug 17 23:44:34	0.46111	12 ^{h} 30 ^{m} 15^s.005	-30 °13 ′04.″766
2017 Aug 17 23:45:51	0.46200	12 ^{h} 25 ^{m} 33^s.996	-31 °13 ′07.″322
2017 Aug 17 23:47:17	0.46300	12 ^{h} 20 ^{m} 53^s.256	-31 °13 ′10.″210
2017 Aug 17 23:48:43	0.46399	12 ^{h} 16 ^{m} 12^s.320	-31 °13 ′11.″223
2017 Aug 17 23:50:09	0.46499	12 ^{h} 11 ^{m} 31^s.649	-31 °13 ′15.″275
2017 Aug 17 23:51:36	0.46600	12 ^{h} 06 ^{m} 50^s.885	-31 °13 ′18.″115
2017 Aug 17 23:53:02	0.46699	12 ^{h} 02 ^{m} 10^s.096	-31 °13 ′24.″372
2017 Aug 17 23:54:28	0.46799	11 ^{h} 57 ^{m} 29^s.387	-31 °13 ′26.″510
2017 Aug 17 23:55:45	0.46888	11 ^{h} 52 ^{m} 48^s.745	-31 °13 ′31.″809
2017 Aug 17 23:57:02	0.46977	11 ^{h} 48 ^{m} 07^s.899	-31 °13 ′33.″279
2017 Aug 17 23:58:28	0.47076	11 ^{h} 43 ^{m} 27^s.248	-31 °13 ′38.″379
2017 Aug 17 23:59:53	0.47175	11 ^{h} 38 ^{m} 12^s.086	-32 °14 ′00.″137
2017 Aug 18 00:01:18	0.47273	11 ^{h} 34 ^{m} 05^s.570	-31 °13 ′47.″746
2017 Aug 18 00:02:35	0.47362	11 ^{h} 29 ^{m} 24^s.922	-31 °13 ′51.″547
2017 Aug 18 00:04:00	0.47461	11 ^{h} 24 ^{m} 44^s.156	-31 °13 ′57.″384
2017 Aug 18 00:05:18	0.47551	11 ^{h} 20 ^{m} 03^s.402	-31 °14 ′02.″252
2017 Aug 18 00:06:35	0.47640	11 ^{h} 15 ^{m} 22^s.440	-31 °14 ′06.″208
2017 Aug 18 00:08:00	0.47738	11 ^{h} 10 ^{m} 41^s.821	-31 °14 ′09.″616
2017 Aug 18 00:09:18	0.47829	11 ^{h} 06 ^{m} 01^s.019	-31 °14 ′16.″647
2017 Aug 18 00:10:35	0.47918	11 ^{h} 01 ^{m} 20^s.029	-31 °14 ′19.″995
2017 Aug 18 00:12:05	0.48022	12 ^{h} 30 ^{m} 13^s.856	-32 °13 ′21.″158
2017 Aug 18 00:13:23	0.48112	12 ^{h} 25 ^{m} 30^s.032	-32 °13 ′23.″827
2017 Aug 18 00:14:40	0.48201	12 ^{h} 20 ^{m} 46^s.426	-32 °13 ′25.″644
2017 Aug 18 00:16:06	0.48301	12 ^{h} 16 ^{m} 02^s.484	-32 °13 ′29.″700
2017 Aug 18 00:17:23	0.48390	12 ^{h} 11 ^{m} 18^s.718	-32 °13 ′32.″247
2017 Aug 18 00:18:40	0.48479	12 ^{h} 06 ^{m} 35^s.049	-32 °13 ′34.″391
2017 Aug 18 00:19:58	0.48569	12 ^{h} 01 ^{m} 51^s.128	-32 °13 ′39.″111
2017 Aug 18 00:21:15	0.48659	11 ^{h} 57 ^{m} 07^s.348	-32 °13 ′43.″128
2017 Aug 18 00:22:32	0.48748	11 ^{h} 52 ^{m} 23^s.580	-32 °13 ′47.″111
2017 Aug 18 00:23:57	0.48846	11 ^{h} 47 ^{m} 39^s.710	-32 °13 ′50.″407
2017 Aug 18 00:25:15	0.48936	11 ^{h} 42 ^{m} 56^s.111	-32 °13 ′54.″176

TABLE 5
Observations of ASA-500 telescope, continued

UT Date	Time Since GW Trigger (days)	Center (R.A.)	Center (Decl.)
2017 Aug 18 00:27:57	0.49124	11 ^{h} 33 ^{m} 28^s.248	-32 °14 ′05″.578
2017 Aug 18 00:29:22	0.49222	11 ^{h} 28 ^{m} 44^s.497	-32 °14 ′08″.661
2017 Aug 18 00:30:39	0.49311	11 ^{h} 24 ^{m} 00^s.649	-32 °14 ′14″.154
2017 Aug 18 00:31:57	0.49402	11 ^{h} 19 ^{m} 16^s.820	-32 °14 ′20″.406
2017 Aug 18 00:33:14	0.49491	11 ^{h} 14 ^{m} 32^s.974	-32 °14 ′23″.645
2017 Aug 18 00:34:31	0.49580	11 ^{h} 09 ^{m} 49^s.015	-32 °14 ′27″.265
2017 Aug 18 00:35:58	0.49681	11 ^{h} 05 ^{m} 05^s.077	-32 °14 ′30″.945
2017 Aug 18 00:37:24	0.49780	11 ^{h} 00 ^{m} 21^s.126	-32 °14 ′35″.378
2017 Aug 18 00:38:54	0.49884	12 ^{h} 30 ^{m} 13^s.123	-33 °13 ′39″.301
2017 Aug 18 00:40:21	0.49985	12 ^{h} 25 ^{m} 26^s.171	-33 °13 ′37″.855
2017 Aug 18 00:41:38	0.50074	12 ^{h} 20 ^{m} 38^s.975	-33 °13 ′44″.215
2017 Aug 18 00:42:55	0.50163	12 ^{h} 15 ^{m} 52^s.081	-33 °13 ′45″.463
2017 Aug 18 00:44:12	0.50252	12 ^{h} 11 ^{m} 05^s.080	-33 °13 ′48″.273
2017 Aug 18 00:45:38	0.50352	12 ^{h} 06 ^{m} 18^s.116	-33 °13 ′51″.389
2017 Aug 18 00:47:04	0.50451	12 ^{h} 01 ^{m} 31^s.219	-33 °13 ′57″.070
2017 Aug 18 00:48:30	0.50551	11 ^{h} 56 ^{m} 44^s.050	-33 °14 ′00″.839
2017 Aug 18 00:49:56	0.50650	11 ^{h} 51 ^{m} 56^s.967	-33 °14 ′04″.169
2017 Aug 18 00:51:21	0.50749	11 ^{h} 47 ^{m} 10^s.057	-33 °14 ′07″.798
2017 Aug 18 00:52:47	0.50848	11 ^{h} 39 ^{m} 19^s.229	-30 °13 ′24″.617
2017 Aug 18 00:52:47	0.50848	11 ^{h} 42 ^{m} 22^s.994	-33 °14 ′11″.486
2017 Aug 18 00:54:13	0.50948	11 ^{h} 37 ^{m} 35^s.838	-33 °14 ′16″.286
2017 Aug 18 00:55:39	0.51047	11 ^{h} 32 ^{m} 49^s.002	-33 °14 ′20″.323
2017 Aug 18 00:57:05	0.51147	11 ^{h} 28 ^{m} 01^s.904	-33 °14 ′23″.832
2017 Aug 18 00:58:31	0.51247	11 ^{h} 23 ^{m} 14^s.613	-33 °14 ′28″.525
2017 Aug 18 00:59:48	0.51336	11 ^{h} 18 ^{m} 27^s.436	-33 °14 ′32″.516

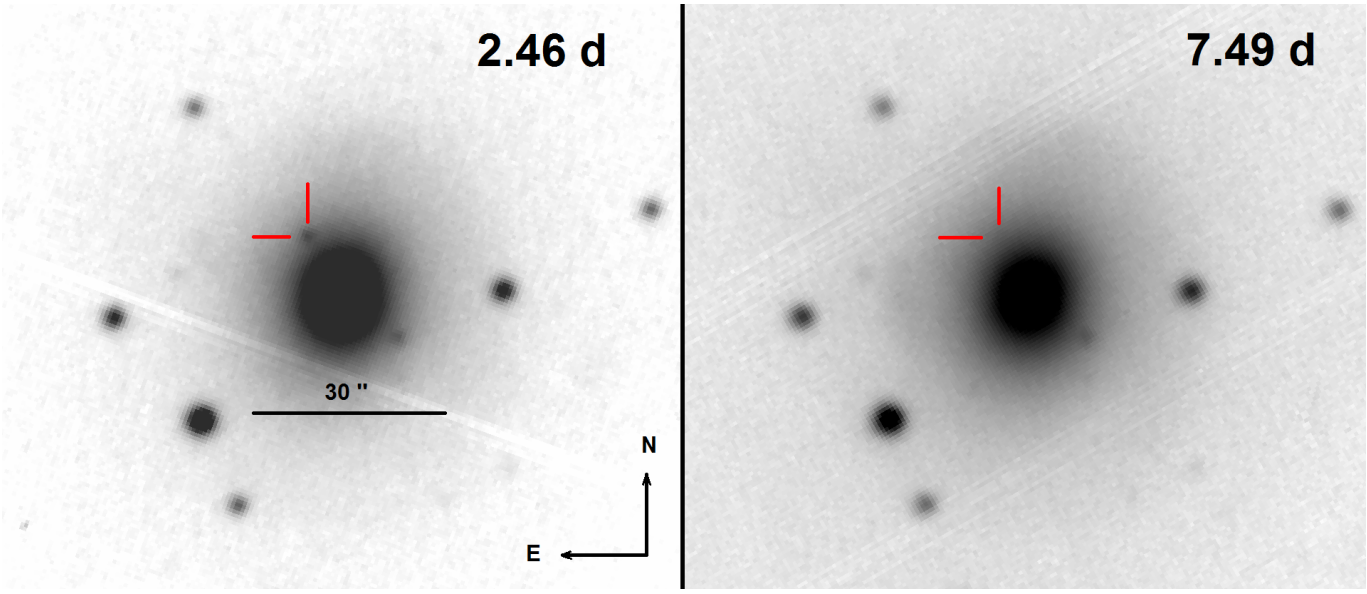

Fig. 10.— Imaging of the SSS17a / AT2017gfo in the outskirts of the NGC 4993 galaxy with Chilescope/RC-1000 in two different epochs. Exposures of both frames are 10 × 180 s in the Clear filter.

The resulting instrumental photometrical magnitudes were calibrated with the USNO-B1.0 catalog R2 magnitudes. After the study of stellar non-saturated objects in the field, we chose four reference stars. The information about them is listed in the Table 7. The results of the photometry are presented in Table 6.

A.6. *Optical light curve*

The light curve of the optical transient, including published so far photometry collected in Villar et al. (2017); Tanvir et al. (2017) in R, r and in J filters is presented the Figure 11. Bold black circles represent the data obtained by RC-1000 telescope in the Clear filter. The data were shifted by 0.25 mag to compensate for the difference between

TABLE 6
Log of the Optical Observations and Photometry of the GW170817.

Date	UT Start	Exposure, s	Elapsed Time, days	R mag.	Error
2017 Aug 19	23:30:33	10×180	2.46157	19.12	0.06
2017 Aug 20	23:21:09	13×180	3.47840	20.04	0.08
2017 Aug 21	23:32:09	22×180	4.49409	20.14	0.12
2017 Aug 24	23:53:39	20×180	7.49278	> 21.0	–

Note. Observations in Clear filter were calibrated against USNO-B1.0 Stars, R2 magnitudes. The magnitudes in the table are not corrected for the Galactic extinction due to the reddening of E(B-V) = 0.109 Schlafly & Finkbeiner (2011) in the direction of the burst.

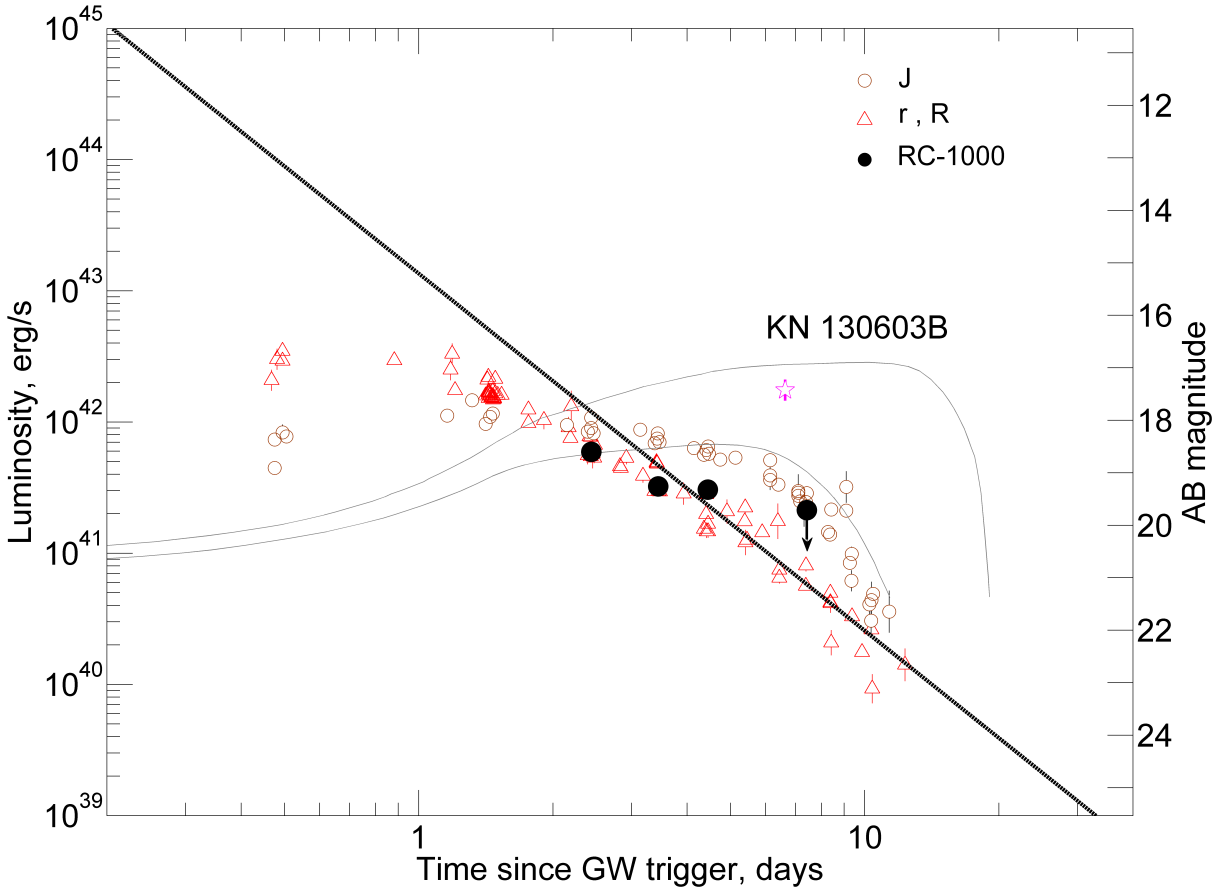

Fig. 11.— Light curve of the OT in units of stellar magnitudes (right Y-axis) and total luminosity $L_{\rm iso}$ (left Y-axis). Bold black circles represent the observations made by the CHILESCOPE/RC-1000 telescope. Red open triangles and brown open circles show r-, R-, and J-band data, respectively, taken from Villar et al. (2017); Tanvir et al. (2017). The optical afterglow approximation of GRB 130603B rescaled to the rest frame is shown by the dashed line. The luminosity of a kilonova associated with GRB 130603B is also shown (purple star). The luminosity is calculated from nIR data obtained in the F160W filter of HST (Tanvir et al. 2013). Thin black curves represent the models from Tanvir et al. (2013), corresponding to ejected masses of $10^{-2}M_{\odot}$ [lower] and $10^{-1}M_{\odot}$ [upper] respectively.

the photometric bands. The shift was calculated using r or R data obtained simultaneously with ours. In the same figure, we plot the nIR afterglow of GRB 130603B (rescaled in both frequency and time) to the rest frame. We used parameters of the afterglow approximation (Flux $\sim t^{-2.72}$) after jet-break at about 0.4 days (Tanvir et al. 2013). The absolute calibration in the rest frame was calculated from the broadband SED of GRB 130603B obtained at ~ 0.6 days post-burst (in the observer frame) in filters $grizJK$ (Table 2 in Tanvir et al. 2013). The plotted afterglow roughly corresponds to the J-filter in the rest frame. For correct calculation of luminosity light curves of GRB 170817A and GRB 130603B we used Galactic extinction in the direction of the bursts, $E(B-V) = 0.109$ and $E(B-V) = 0.02$, correspondingly (Schlafly & Finkbeiner 2011). A host galaxy extinction was not taken into account. It is evident from Figure 11 that the afterglow luminosity of GRB 170817A is more than 130 times fainter than that of GRB 130603B in the J-filter.

TABLE 7
Reference Stars Used for the Photometrical Reduction.

USNO-B1.0 ID	R.A.	Decl.	USON-B1.0 R2 mag.	PanSTARRS r mag. (err)
0665-0279047	13:09:34.72	-23:24:45.9	17.26	17.474 (0.004)
0666-0290876	13:09:49.74	-23:20:34.6	16.51	16.812 (0.006)
0666-0290916	13:10:04.58	-23:20:47.8	17.23	17.466 (0.009)
0665-0279123	13:09:54.37	-23:25:34.3	16.89	17.224 (0.014)

B. BSA: RADIO OBSERVATIONS AT 110 MHZ

One of the most sensitive radio telescopes at the frequency of 110 MHz is the Big Scanning Antenna (BSA, Puschino, Russia). BSA is a radio telescope of meridian type. The BSA observation is a continuous survey in multibeam mode in the frequency range of 109.0–111.5 MHz using 96 beams covering a field of view from −8 and up to +42° in decl. with a time resolution of 12.5 ms (Samodurov et al. 2017).

The form of the BSA single beam diagram is described by the function

$$(\alpha, \delta) = \left(\frac{\sin x}{x}\right)^2 \cdot \left(\frac{\sin y}{y}\right)^2, \tag{B1}$$

where $x = (\pi D_1/\lambda) \cdot (\alpha - \alpha_0)$, $y = (\pi D_2 \cos(Z)/\lambda) \cdot (\delta - \delta_0)$, α and δ are equatorial coordinates, (α_0, δ_0) are the coordinates determining the position of the maximum of the diagram directionality of the radio telescope, $D_1 = 384$ m and $D_2 = 187$ m are the dimensions of BSA in the direction from north to south, and from east to west, respectively, $\lambda = 2.72$ m is a wavelength, Z is the angle between direction to object and antenna normal. It can be found from (B1) that the size of the primary beam is about 50 arcmin in R.A. (or nearly 5 minutes) and about 30 arcmin in decl.

The OT position at the time of the GW170817 trigger was 11°.5 above horizon at the BSA location, but outside the BSA multibeam diagram, that is, 15° lower in decl. and 4° (or 14 minutes in R.A.) east from the BSA pointing direction. BSA can detect radio transients around twentieth side lobes of southern beams if the transient would be sufficiently bright. It can be found from (B1) that the twentieth side lobe has an efficiency of about $3 \cdot 10^{-4}$. However, (B1) is the formula for ideal antenna. Really, bright radio sources such as Sun or Cygnus A (3C 405) are indeed registered in side lobes of BSA at a distance of ±40° with an efficiency of $\sim 10^{-3}$ and at a distance of ±10° with an efficiency of $\sim 10^{-2}$. As a result, we use side lobe efficiency of 10^{-2} in our calculation. Details of side lobe BSA calibration can be found elsewhere (V. Samodurov et al. 2018, in preparation).

We investigated all data sets around the GW170817 trigger recorded with BSA. The only significant transient signal with a duration of 1.5 s centered at (UTC) 12:47:44.7 of about 100 Jy was detected in the southern beams at 109.273-111.148 MHz (see Figure 12). We mostly believe the signal has a non-astrophysical nature because of the lack of a dispersion pattern, which is specific for distant astrophysical objects such as, e.g., pulsars. We can place a conservative upper limit of 30 Jy (it is equivalent to S/N> 10) on a time scale of 10-60 s for any astrophysical signal.

We can estimate the intensity of the possible astrophysical signal, which can be detected by side lobes at the time of the GW170817 trigger. The FWHM of the side lobe along R.A. is about 5 minutes. The OT position was 2.5×FWHM of the diagram at the trigger time of GW170817. Using a projection of the BSA array toward the OT ($cos(78.65) = 0.2$) and side lobe efficiency $\sim 10^{-2}$, we estimate the upper limit on the transient radio signal from the position of the OT as 15000 Jy. The value can be converted into the upper limit of a luminosity of the radio transient at the distance of the OT $L_{(\mathrm{iso})}^{110\mathrm{Mhz}} < 5 \times 10^{40}$ erg s^{-1} for a duration of the transient in the range of 10-60 s.

C. SPI-ACS/INTEGRAL DATA ANALYSIS

SPI-ACS experiment consisting of 91 BGO crystals is operating in a single energy channel with a lower threshold of ~ 80 keV and time resolution of 50 ms (von Kienlin et al. 2003). A script[8] was used as the source of input SPI-ACS data.

GRB 170817A was detected in SPI-ACS at a 4.5σ significance level. The burst onset is delayed to GW trigger to $\simeq 2$ s. A third-order polynomial model was used to fit background signal in time intervals $(-118, -30)$ s and $(300, 900)$ s (data before −118 s are not available). We found for GRB 170817A that there is a deviation of SPI-ACS count statistics from Poisson distribution with a factor of $\simeq 1.26$ (see, e.g., Minaev et al. 2010a; Minaev & Pozanenko 2017). Statistical uncertainties for SPI-ACS data were estimated, taking into account the factor of deviation.

We found the duration of the burst in SPI-ACS data, $T_{90}^{ACS} = 1.0 \pm 0.4$ s, to be significantly longer comparing with $T_{90} \simeq 0.1$ s derived in Savchenko et al. (2017a). Our value is more consistent with GBM results obtained in our paper (see Figure 1 and Section 3.2) and in Goldstein et al. (2017a). The duration, $T_{90} = 1.0 \pm 0.4$ s, characterizes the burst to be from a short (or type I) population with a probability of $\sim 74\%$ (see Fig. 11 in Minaev & Pozanenko 2017).

The burst fluence calculated for the (2, 3) s time interval since the GW trigger is $F = (1.8 \pm 0.4) \times 10^3$ counts. The off-axis for the GRB 170817A source from the satellite pointing axis is 105 deg, which is quite optimal for detection. In the paper by Viganò & Mereghetti (2009), it was shown that 1 SPI-ACS count corresponds on average to $\approx 10^{-10}$erg cm^{-2} in the (75, 1000) keV range, for directions orthogonal to the satellite pointing axis. Using the conversion factor,

[8] http://isdc.unige.ch/~savchenk/spiacs-online/spiacs-ipnlc.pl

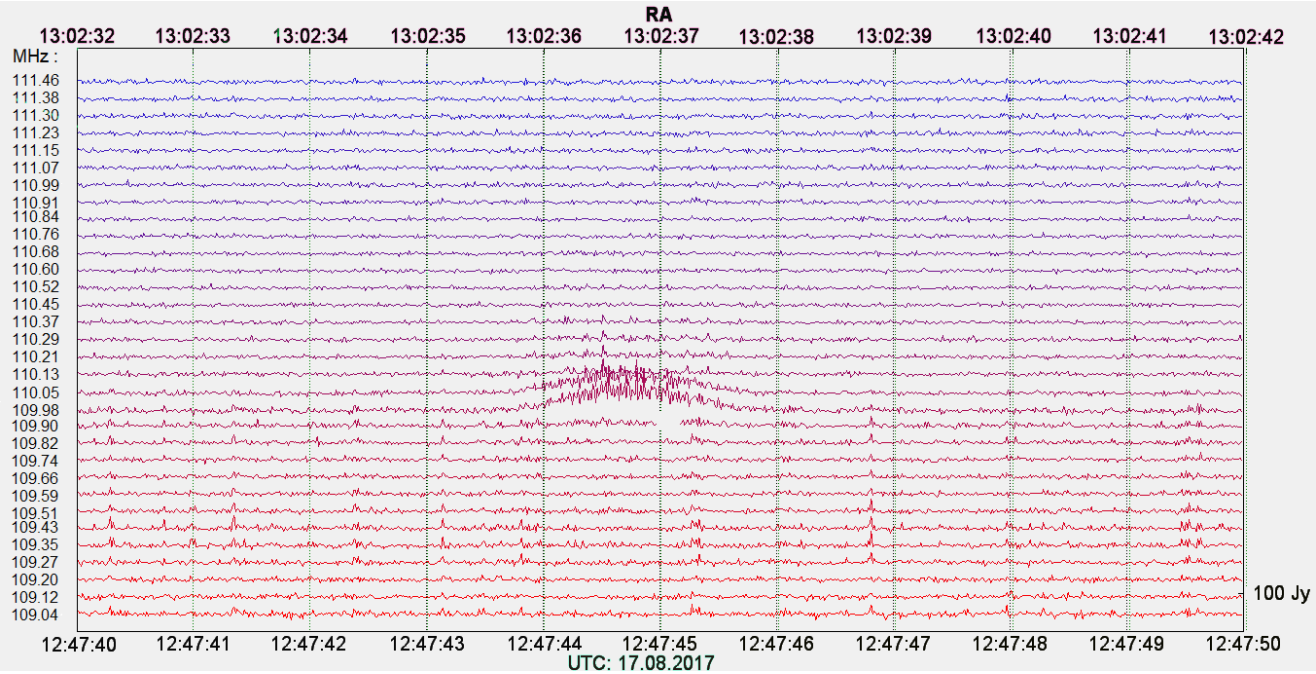

FIG. 12.— BSA observation at 109 - 110.25 MHz frequency channels (Y-axis) around the GW170817 trigger time (lower X-axis). In particular, in the shown beam toward decl. ($J2000$) $= -4.82$ the nearly symmetric signal is visible at frequency channels from 109.898 and up to 110.367 MHz. The signal is visible in the southern beams and centered at (UTC) 12:47:44.7 i.e. 400 s later than the GW170817 trigger time. This is the most powerful signal of about 100 Jy detected during 15 minutes since the GW170817 trigger. It most likely has an artificial origin.

we derive $F = (1.8 \pm 0.4) \times 10^{-7}$ erg cm^{-2} in the (75, 1000) keV range for GRB 170817A. This value is in agreement with one estimated in Savchenko et al. (2017a) using a more complex method.

We did not find any precursor or extended emission components in SPI-ACS data at time scales from 0.05 up to 100 s in the time interval (-50, 200) s since the GW trigger and we estimated upper limits on their intensity. At a time scale of 0.05 s, the upper limit on precursor activity is $S_{\rm prec} \simeq 250$ counts or $S_{\rm prec} \simeq 2.5 \times 10^{-8}$ erg cm^{-2} at the 3σ significance level. At a time scale of 50 s, the upper limit on extended emission activity is $S_{\rm EE} \simeq 8100$ counts or $S_{\rm EE} \simeq 8.1 \times 10^{-7}$ erg cm^{-2} at the 3σ significance level.

Assuming redshift z = 0.00968 and luminosity distance $D_L = 42.0$ Mpc for the source (Jones et al. 2009), we estimated total isotropic energy release in the energy range (75, 1000) keV as $E_{\rm iso} = (3.9 \pm 0.9) \times 10^{46}$ erg. One can estimate the upper limits on the precursor and extended emission component expressed as total isotropic energy release as well: $E_{\rm iso}^{\rm prec} = 5.3 \times 10^{45}$ erg and $E_{\rm iso}^{\rm EE} = 1.7 \times 10^{47}$ erg, correspondingly.

D. MAGNETIC FORCE-FREE BOMB

At the moment of the breakout, the jet, which was strongly magnetically dominated close to the BH but became mildly magnetically dominated during the confined propagation (Section 4.1), starts to expand and accelerate. As the pair density falls precipitously, the flow becomes more and more magnetically dominated. In this appendix, we consider the explanation of a magnetic force-free bomb – radial motion of the post-breakout highly magnetized plasma flows.

Consider the radial expansion of force-free plasma carrying the toroidal magnetic field. The relativistic force-free condition implies that the total EM force vanishes (Gruzinov 1999)

$$\mathbf{E}\,\nabla\cdot\mathbf{E} + \mathbf{J}\times\mathbf{B} = 0 \to \mathbf{J} = \frac{(\mathbf{E}\times\mathbf{B})\nabla\cdot\mathbf{E} + (\mathbf{B}\cdot\nabla\times\mathbf{B} - \mathbf{E}\cdot\nabla\times\mathbf{E})\mathbf{B}}{B^2}, \tag{D1}$$

(for the GR formulation, see Komissarov 2011; Lyutikov 2011c).

Separating the angular and the time-radial dependence, $B_\phi = B_\phi(t,r)b_\phi(\theta)$ and $E_\theta = E_\theta(t,r)e_\theta(\theta)$, we find two types of solutions. The first is the solution self-similar in $Z = r/t$,

$$\begin{aligned} &E_\theta(Z) = B_\phi(Z) = (1-1/Z)B_0,\\ &e_\theta(\theta) = b_\phi(\theta),\\ &j_r = (1-1/Z)\frac{\partial_\theta(b_\phi\sin\theta)}{r\sin\theta},\\ &\nabla\cdot\mathbf{E} = (1-1/Z)\frac{\partial_\theta(b_\phi\sin\theta)}{r\sin\theta} = j_r. \end{aligned} \tag{D2}$$

Equation (D2) represents solutions for the polar-angle-dependent expansion of force-free plasma into vacuum. Poynting flux is zero at the edge of the outflow at $r = t$ and increases for smaller r. If the source is located at $r \ll t$, it is required that the source luminosity increases with time $\propto t^2$ for the solution to be applicable.

Second, looking for a solution of the type $B_\phi, E_\theta \propto 1/r$, we find that the following scaling satisfies the Maxwell equations

$$B_\phi(t,r) = E_\theta(t,r) = \frac{f(t-r)}{r},$$
$$j_r = \frac{f(t-r)}{r^2}\frac{\partial_\theta(b_\phi \sin\theta)}{r\sin\theta} \tag{D3}$$

where f is an arbitrary function of the argument. This solution represents a force-free pulse of initial shape $f(r)$, moving with the speed of light – a force-free bomb.

Both solutions (D2) and (D3) are different from EM fields in vacuum since there are non-zero currents and charge densities in the flow. A general time-dependent approach to force-free fields for the specific case of $\rho = j$ has been discussed by Gralla & Jacobson (2014); see Lyutikov (2011b) for a related time-dependent solution in general relativity.